NeuroImage 187 (2019) 32–55

Contents lists available at ScienceDirect

NeuroImage

journal homepage: www.elsevier.com/locate/neuroimage

Imaging vascular and hemodynamic features of the brain using dynamic susceptibility contrast and dynamic contrast enhanced MRI

C. Chad Quarles *, Laura C. Bell, Ashley M. Stokes

Division of Neuro imaging Research, Barrow Neurological Institute, 350 W. Thomas Rd, Phoenix, AZ, USA

ARTICLE INFO

Keywords:
Dynamic susceptibility contrast MRI
Dynamic contrast enhanced MRI
Perfusion
Vascular permeability

ABSTRACT

In the context of neurologic disorders, dynamic susceptibility contrast (DSC) and dynamic contrast enhanced (DCE) MRI provide valuable insights into cerebral vascular function, integrity, and architecture. Even after two decades of use, these modalities continue to evolve as their biophysical and kinetic basis is better understood, with improvements in pulse sequences and accelerated imaging techniques and through application of more robust and automated data analysis strategies. Here, we systematically review each of these elements, with a focus on how their integration improves kinetic parameter accuracy and the development of new hemodynamic biomarkers that provide sub-voxel sensitivity (e.g., capillary transit time and flow heterogeneity). Regarding contrast mechanisms, we discuss the dipole-dipole interactions and susceptibility effects that give rise to simultaneous T_1, T_2 and T_2^* relaxation effects, including their quantification, influence on pulse sequence parameter optimization, and use in methods such as vessel size and vessel architectural imaging. The application of technologic advancements, such as parallel imaging, simultaneous multi-slice, undersampled k-space acquisitions, and sliding window strategies, enables improved spatial and/or temporal resolution of DSC and DCE acquisitions. Such acceleration techniques have also enabled the implementation of, clinically feasible, simultaneous multi-echo spin- and gradient echo acquisitions, providing more comprehensive and quantitative interrogation of T_1, T_2 and T_2^* changes. Characterizing these relaxation rate changes through different post-processing options allows for the quantification of hemodynamics and vascular permeability. The application of different biophysical models provides insight into traditional hemodynamic parameters (e.g., cerebral blood volume) and more advanced parameters (e.g., capillary transit time heterogeneity). We provide insight into the appropriate selection of biophysical models and the necessary post-processing steps to ensure reliable measurements while minimizing potential sources of error. We show representative examples of advanced DSC- and DCE-MRI methods applied to pathologic conditions affecting the cerebral microcirculation, including brain tumors, stroke, aging, and multiple sclerosis. The maturation and standardization of conventional DSC- and DCE-MRI techniques has enabled their increased integration into clinical practice and use in clinical trials, which has, in turn, spurred renewed interest in their technological and biophysical development, paving the way towards a more comprehensive assessment of cerebral hemodynamics.

Abbreviations: CA, contrast agent; DSC, dynamic susceptibility contrast; DCE, dynamic contrast enhanced; CBV, cerebral blood volume; CBF, cerebral blood flow; MTT, mean transit time; BBB, blood brain barrier; SE, spin echo SE; gradient echo, GRE; vessel size imaging, VSI; vessel architectural imaging, VAI; short echo times, TE; repetition time, TR; spin and gradient echo, SAGE; contrast to noise ratio, CNR; arterial input function, AIF; echo planar imaging, EPI; principles of echo shifting with a train of observations, PRESTO; perfusion with multiple echoes and temporal enhancement, PERMEATE; sensitivity encoding, SENSE; generalized autocalibrating partial parallel acquisition, GRAPPA; simultaneous multi-slice, SMS; golden-angle radial sparse parallel, GRASP; simplified SAGE, sSAGE; spiral perfusion imaging with consecutive echoes, SPICE; partial volume effects, PVE; variable flip angle, VFA; look-locker, LL; spoiled gradient-echo sequences, SPGR; capillary transit time heterogeneity, *CTH*; apparent diffusion coefficient, *ADC*; normal appearing white matter, NAWM; time-to-maximum, T_{max}; time-to-peak, *TTP*; initial area under the curve, *iAUC*; percent signal recovery, *PSR*; region of interest, ROI.

* Corresponding author. Neuroimaging Research Barrow Neurological Institute, 350 W. Thomas Rd Phoenix, AZ 85013, USA.
E-mail address: chad.quarles@barrowneuro.org (C.C. Quarles).

https://doi.org/10.1016/j.neuroimage.2018.04.069
Received 1 October 2017; Received in revised form 27 April 2018; Accepted 29 April 2018
Available online 3 May 2018
1053-8119/

Mathematical symbols

T_1	spin-lattice relaxation time
T_2	spin-spin relaxation time
T_2^*	effective T_2 reflecting magnetic field inhomogeneities
R_2^*	T_2^* relaxation rate
R_2	T_2 relaxation rate
R_1	T_1 relaxation rate
r_1 :	contrast agent T_1 relaxivity
r_2	contrast agent T_2 relaxivity
r_2^*	contrast agent T_2^* relaxivity
ΔR_2^*	the contrast agent induced change in R_2^* from baseline
ΔR_2	the contrast agent induced change in R_2 from baseline
ΔR_1	the contrast agent induced change in R_1 from baseline
TE	pulse sequence echo time
TR	pulse sequence repetition time
$\propto$	pulse sequence flip angle
B_o	static magnetic field strength
S_{TE_x} :	MRI signal from a multi-echo sequence for TE = x
$C_t(t)$	tissue contrast agent concentration time profile
$C_{AIF}(t)$:	arterial input function
$R(t)$:	residue function
$h(t)$:	transport function
ρ :	brain tissue density
H_f	hematocrit
A	arterial input function matrix
R	residue function matrix
C	tissue concentration time curve
S_0^I	baseline signal intensity of a SAGE acquisition before the 180° pulse
S_0^{II}	baseline signal intensity of a SAGE acquisition after the 180° pulse
δ	parameter to quantify slice-profile mismatch in a SAGE dataset
γ	gyromagnetic ratio of the protons
$\Delta\chi$	susceptibility difference
Q	vessel density
VSI	vessel size index
mVD	mean vessel diameter
K^{trans}	contrast agent volume transfer constant between blood plasma and the extravascular extracellular space
Ve	volume fraction of the extravascular extracellular space

Introduction

Contrast enhanced MRI methods are widely used to interrogate hemodynamic and vascular properties of brain tissue, including pathologic conditions such as cancer, stroke, and other neurological disorders. Such studies involve the intravenous administration and serial tracking of MRI contrast agents through the cerebral circulation and, in the case of a disrupted blood brain barrier, the interstitial space. The intrinsic relaxation times (T_1, T_2 and T_2^*) of tissue water are shortened by the passage of contrast agent (CA), leading to detectable changes in the MRI signal. The two most commonly used contrast enhanced methods are divided based on the affected MR relaxation time, where dynamic contrast enhanced (DCE) MRI studies (Yankeelov and Gore, 2009) are designed to track changes in tissue T_1 and dynamic susceptibility contrast (DSC) MRI methods (Willats and Calamante, 2013) rely on CA induced T_2 (or T_2^*) changes. Pharmacokinetic and/or biophysical models are applied to the acquired DCE- and/or DSC-MRI signal time courses to estimate functional and structural features of the tissue vasculature (Ostergaard et al., 1996b; Tofts et al., 1999). Numerous studies have established the utility of DCE- and DSC-MRI biomarkers for diagnosis, prognostication, and therapeutic response assessment in the clinic and in the context of multi-institutional clinical trials. Given the maturation of DSC- and DCE-MRI and their increased clinical use, multiple national initiatives have established (or are working towards) standardized acquisition and analysis protocols (e.g. (QIBA, 2012; Welker et al., 2015)).

As with most imaging technologies, the clinical applicability, interpretation, and fidelity of the derived DSC- and DCE-MRI parameters depends on three elements: 1) an appropriate understanding of the method's biophysical basis, 2) the methods used to acquire the data and 3) the MRI signal and kinetic analysis of the measured data. Over two decades of research have been devoted to characterizing the fundamental contrast mechanisms underlying contrast enhanced MRI, optimizing the pulse sequences to increase contrast to noise and temporal and spatial resolution, and developing post-processing strategies that maximize the clinical accuracy of the extracted parameters. In addition, the advancement and synergistic integration of these three elements, along with improved MR hardware, have enabled the simultaneous interrogation of new structural and physiological biomarkers of interest. This paper reviews these three essential elements of DSC- and DCE-MRI methodology, with a particular focus on recent advancements.

Biophysical basis of DSC- and DCE-MRI

Unlike other imaging modalities (e.g., CT) contrast enhanced MRI is unique in that it does not directly detect the injected CAs. Instead, the change in the MRI signal reflects the influence of the CA on the local relaxation times of water. The indirect detection of CA through measured changes in MRI signal introduces challenges to quantification. As illustrated in Fig. 1A, CA infusion can lead to two disparate effects: direct microscopic (on the order of a molecule size) interaction of CA with water and through-space mesoscopic (on the order of the cell or vessel size) effects induced by CA compartmentalization. Accordingly, the degree to which tissue T_1, T_2 and T_2^* are shortened reflects a combination of the CA concentration, its magnetic properties, its distribution within tissue compartments, the local microstructure (e.g., vascular and cellular architecture), water diffusion, and water exchange across cellular membranes. The changes in relaxation times yield the representative DSC-MRI (T_2^*-weighted) and DCE-MRI (T_1-weighted) signals shown in Fig. 1B–C.

Contrast agent biodistribution

The biodistribution of CA in tissue largely determines the biophysical basis of the mechanism of relaxation time changes. Most clinically approved CAs for MRI are small molecular weight compounds (0.5–1 kD) that are freely diffusible and, after injection, will travel through the vasculature and pass into the interstitium (Caravan et al., 1999). An exception is in normal brain tissue, where the blood brain barrier (BBB) largely prevents extravasation. As detailed below (section 2.6), compartmentalization of CA within the vasculature, due to an intact BBB, predominantly influences T_2 (or T_2^*) times (as illustrated by the lower blood vessel in Fig. 1A and reflected in the signal shown in Fig. 1C) and is typically assumed with conventional DSC-MRI methodology (Boxerman et al., 1995). In many neuropathologies (e.g., brain cancer, stroke, multiple sclerosis), the BBB is disrupted and CA can diffuse into the extravascular space. The distribution of a CA across the vasculature and interstitium, due to BBB leakage, can lead to additional changes in T_1 (section 2.3), leading to the representative signal in Fig. 1B, that can be quantified with DCE-MRI (Tofts et al., 1999). In neuroclinical practice, DCE-MRI is rarely used when the BBB is intact. However, DSC-MRI is used to assess hemodynamics in both normal and diseased tissue, the

latter requiring specialized acquisition and/or analysis strategies to minimize or correct for the effects of CA leakage (as illustrated by the upper blood vessel in Fig. 1).

Contrast agent relaxivity

The relaxivity of a CA is a measure of its ability to modulate proton relaxation rates ($1/T_1$, $1/T_2$, or $1/T_2^*$) as a function of concentration, with units of $mM^{-1}s^{-1}$. A linear relationship between CA concentration and relaxation rate (e.g., $R_1 = 1/T_1$) is often assumed (Tóth et al., 2002):

$$R_i(t) = r_i \cdot C_t(t) + R_{io} \quad (1)$$

where "i" is equal to 1, 2, or 2* and denotes the three different relaxation rates (R_1, R_2 *and* R_2^*), R_{io} and $R_i(t)$ are the pre- and post-contrast relaxation rates, respectively, $C_t(t)$ is the dynamic CA concentration in the tissue, and r_i is the CA relaxivity. Note that each relaxation mechanism has a unique contrast agent relaxivity (r_1, r_2 and r_2^*) and their magnitude depends on field strength. As expected, for a given concentration in a tissue of interest, a CA with a higher relaxivity will induce a greater change in the relaxation rate. In DSC-MRI, this relaxivity value is unknown (for reasons that will be described in Section 2.5); in practice, it is either ignored or given a value based on prior simulations (Willats and Calamante, 2013). In DCE-MRI, the CA relaxivity values are measured *in vitro*. For simplicity, CA relaxivity values are typically assumed to be constant across patients and tissue types, but are known to vary with a tissue's macromolecular composition (Stanisz and Henkelman, 2000).

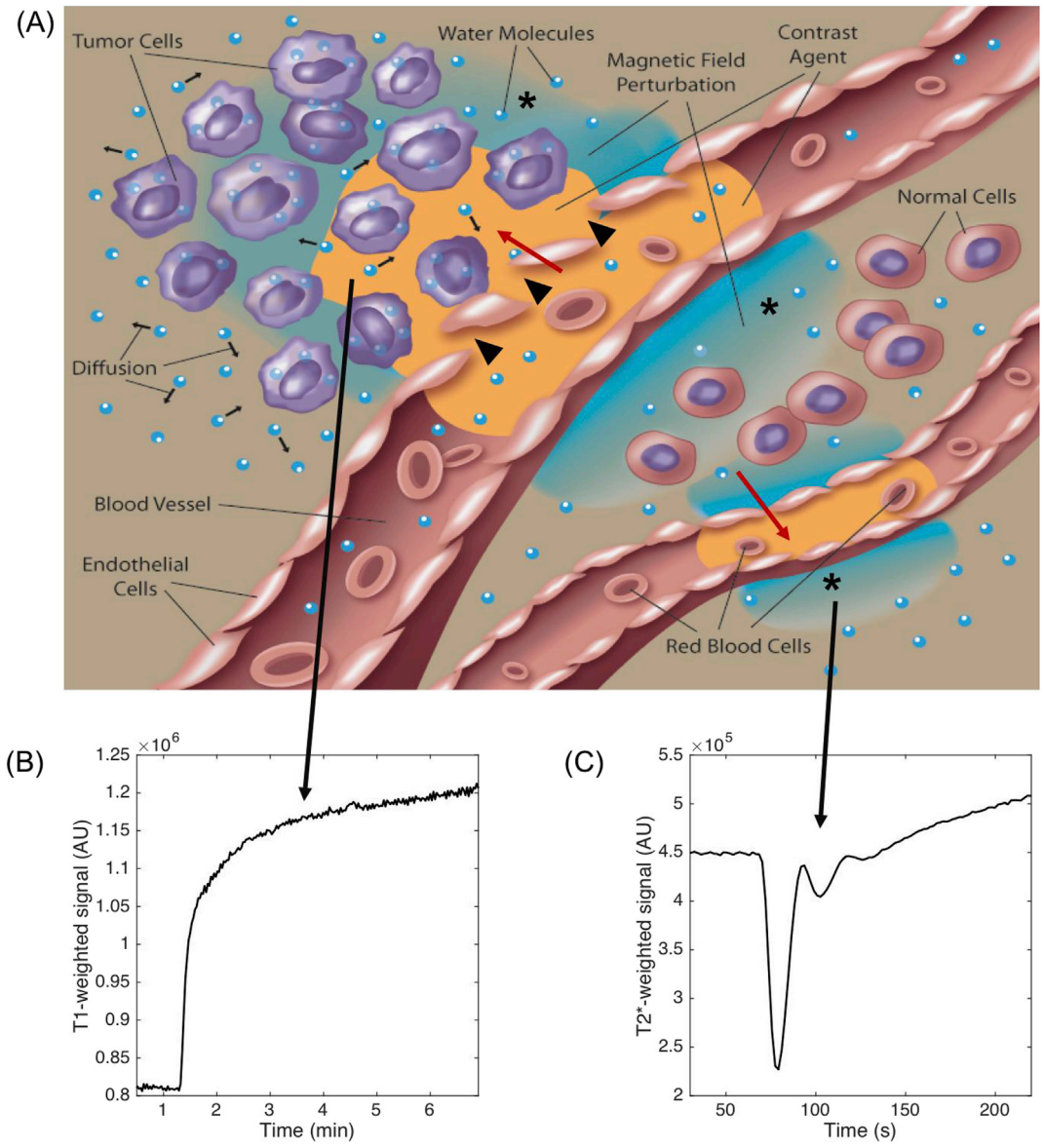

Fig. 1. Illustration of CA distribution within tissue, its interaction with water protons (**A**) and the induced T_1-weighted (**B**) or T_2^*-weighted (**C**) signal changes. When the blood brain barrier is intact, as illustrated in the lower blood vessel, the CA only has direct access to intravascular water (red arrow) so that the associated change in the effective tissue T_1 is small. However, if the blood brain barrier is disrupted (top blood vessel, black triangles) the CA distribution and microscopic interaction with water within the extravascular space (red arrow) substantially decreases tissue T_1 and increases a T_1-weighted signal (B), like that used for DCE-MRI. The compartmentalization of CA in blood (lower blood vessel) or in the extravascular extracellular space (top blood vessel) gives rise to mesoscopic magnetic field gradients surrounding these compartments (as denoted by the asterisks). The diffusion of water through these fields (small black arrows) decreases T_2^* and a

Paramagnetic contrast agents and dipole-dipole interactions

Most clinical MRI CAs are Gadolinium (Gd)-based chelates due to the large dipole moments of paramagnetic metal ions. Since none of Gd's seven unpaired electrons are involved in bonding, the large magnetic moment of Gd is preserved even when it is chelated to ligands, a necessary step owing to the toxicity of free Gd. The resulting magnetic moment of these electrons, which is 660 times higher than that of a proton due to their smaller mass, generates fluctuating microscopic magnetic fields that interact with those of water protons, leading to a change in proton relaxation. The theoretical and molecular basis of dipole-dipole interactions and lanthanide based CAs has been described extensively in the literature (Aime et al., 1998; Belorizky et al., 2008; Bloembergen and Morgan, 1961; Caravan et al., 1999; De Leõn-Rodríguez et al., 2015; Lauffer, 1987).

Given the microscopic distance over which dipole-dipole interactions occur, the net effect on tissue relaxation enhancement will largely depend on a CA's biodistribution. When the BBB is intact and the CA is confined to the vasculature, only the protons within the blood are affected (assuming slow water exchange across the endothelial wall). In such cases, only 2–4% of tissue water, the fractional blood volume range in normal white and gray matter (Leenders et al., 1990), will experience relaxation enhancement, while intracellular and interstitial protons remain unaffected. In order to reliably detect such changes with DCE-MRI the relaxivity of the CA would have to be substantially higher than those in current clinical use, which explains the limited use of DCE-MRI to pathologies that disrupt the BBB.

Superparamagnetic contrast agents

Another class of MRI CAs are iron-oxide nanoparticles (Renshaw et al., 1986; Wang et al., 2001; Weissleder et al., 1995), whose core can contain several thousand Fe ions. Such nanoparticles are superparamagnetic due to their single-domain nature, which in the presence of a magnetic field yields a net magnetic moment that far exceeds that of a single paramagnetic atom. These nanoparticles form the basis of potent vascular imaging agents for MR angiography because their size (e.g. 20–100 nm) prevents extravasation over the course of a typical MRI exam. The real value of these blood pool nanoparticles originates from their substantial T_2 and T_2^* relaxivity, which can be an order of magnitude higher (e.g. $>100\,mM^{-1}sec^{-1}$) than that measured for Gd-based agents, rendering them highly effective for DSC-MRI studies (Bjørnerud et al., 2002; Tong et al., 2010). The marked increase in T_2 and T_2^* relaxivity exhibited by iron oxide nanoparticles is due to susceptibility contrast, a mechanism distinct from dipole-dipole interactions. The T_1 relaxivity of commercially available iron oxide nanoparticles is higher than Gd-based agents, with values reported up to $25\,mM^{-1}sec^{-1}$ (Rohrer et al., 2005). Even with enhanced T_1 relaxivity from dipole-dipole effects, iron-oxide nanoparticles are rarely used for DCE-MRI studies. However, recent studies have demonstrated the use of ultrashort time-to-echo (UTE) sequences for DCE-MRI with iron-oxide-based CAs (Gharagouzloo et al., 2015; Rivera-Rivera et al., 2018).

While there are currently no iron-oxide nanoparticles approved for MRI, ferumoxytol is clinically indicated for iron replacement therapy in patients with anemia and can be used, off-label, for a wide range of MRI applications (Vasanawala et al., 2016). Moreover, it is under evaluation as a contrast agent for DSC-MRI in multiple clinical trials (NCT009785562, NCT00660543, NCT00103038). The T_1 and T_2^* relaxivities of ferumoxytol are 15 and $89\,mM^{-1}s^{-1}$, respectively (Corot et al., 2006). Ferumoxytol-based DSC-MRI maps of CBV have shown potential for differentiating pseudoprogression from treatment response in pediatric and adult brain tumor patients (Gahramanov et al., 2013; Nasseri et al., 2014; Thompson et al., 2012).

Magnetic susceptibility effects

While dipole-dipole interactions are the predominant source of CA-induced T_1 relaxation enhancement in DCE-MRI, susceptibility effects are the predominant contrast mechanism responsible for DSC-MRI signal changes. The underlying theoretical basis of susceptibility effects arising from exogenous CAs has been well characterized (Boxerman et al., 1995; Frøhlich et al., 2005; Kiselev, 2001; Villringer et al., 1988; Weisskoff et al., 1994). The unequal distribution of CA, either Gd- or nanoparticle-based, in tissue gives rise to susceptibility differences between tissue compartments (e.g. intra- and extra-vascular space) that induce mesoscopic magnetic field gradients. These field inhomogeneities accelerate loss of phase coherence (and signal on T_2- and T_2^*-weighted images) due to increased variability in local resonance frequencies experienced by protons as well as their diffusional motion. While dipole-dipole interactions occur over distances of nanometers, these magnetic field inhomogeneities can extend over several micrometers, thereby affecting many more protons and yielding CA relaxivity values that can be an order of magnitude larger than T_1 relaxivity. For example, the T_2^* relaxivity of clinical Gd-based CAs, when compartmentalized within capillaries, is on the order of $80\,mM^{-1}sec^{-1}$ (Kjolby et al., 2006). Even with the enhanced T_2^* relaxivity, DSC-MRI studies are intentionally designed to maximize these susceptibility effects through the use of rapid bolus injections and high temporal resolution imaging (~1–2 s), in order to capture the tracer's first pass through tissue when the concentration is the highest.

DSC-MRI quantification

As described in Section 2.2, the application of Equation (1) to DSC-MRI data assumes that the CA relaxivity (r_2 and r_2^*) for spin- and gradient-echo based DSC-MRI data, respectively) is constant and linear across the brain and pathologies. However, it is well understood that vascular architecture influences CA-based magnetic field inhomogeneities, such that the resulting contrast agent relaxivity could vary across normal brain tissue and certainly varies in cases of pathology (e.g., tumor angiogenesis). For example, in a computational study evaluating the influence of vascular morphology on T_2^* relaxivity, it was found that by expanding the range of possible branching angles in a fractal-based vascular tree to match the abnormalities observed in brain tumors, the relaxivity varied three-fold (Semmineh et al., 2014). In a pre-clinical brain tumor model, tumor vascular relaxivity was shown to be approximately half that found in normal cortical tissue (Pathak et al., 2002). While vascular relaxivity differences are readily apparent in the context of highly abnormal brain tumor vasculature, the differences across normal tissue are less substantial. In a cohort of eight volunteers, significant correlations between regional *CBV* data at rest and under hypocapnic conditions were demonstrated across DSC-MRI and SPECT imaging of 99mTc-labeled red blood cells (an established reference), demonstrating the validity of DSC-MRI, even without local quantification of vascular relaxivity (Engvall et al., 2008). By extension, heterogeneous vascular relaxivity should not confound DSC-MRI across most neurologic disorders since they do not extensively modify normal vascular architecture.

Contrast agent extravasation

A central assumption in DSC-MRI is that CA will remain confined inside blood vessels over the course of its passage through tissue. If the BBB is disrupted the CA will extravasate and distribute around cells in the interstitium, giving rise to pronounced T_1 effects as described in Section 2.3. Leakage of CA will also reduce the susceptibility difference between the intra- and extravascular space because the difference in the concentration between these compartments is lowered. This effectively lowers the CA T_2^* relaxivity and renders it temporally variant since the susceptibility effects at each time point after injection will be a function of the difference in the concentration in the plasma and interstitium (Quarles

et al., 2009; Sourbron et al., 2009). The compartmentalization of CA around cells (as illustrated in Fig. 1) also induces additional mesoscopic magnetic field gradients and greater T_2^* signal losses. Similar to the influence of vascular architecture on susceptibility effects, these additional CA T_2^* leakage effects depend on the interstitial microstructure, which is predominantly determined by cellular features like density, size, shape, atypia and polydispersity (Semmineh et al., 2015). This sensitivity to cellularity is responsible for the characteristic DSC-MRI signal differences observed across different brain tumor types, where primary central nervous system lymphomas and brain metastasis predominantly exhibit strong post-bolus T_1 and T_2^* leakage effects, respectively (Mangla et al., 2011). It should be noted that CA leakage effects are known to reduce the reliability (and clinical utility) of DSC-MRI measures of *CBV* (Boxerman et al., 2006) but there are a wide range of acquisition and post-processing methods that can minimize their influence (Bjornerud et al., 2011; Boxerman et al., 2012; Donahue et al., 2000; Hu et al., 2015; Leu et al., 2016; Quarles et al., 2005; Stokes et al., 2016a).

Spin and gradient echo sensitivity to susceptibility effects

The sensitivity of DSC-MRI to microstructure-dependent magnetic field inhomogeneities also depends on whether gradient echo (GRE) or spin echo (SE) pulse sequences are used to acquire the data. DSC-MRI signals acquired with a GRE sequence experience larger signal loss, and thus greater contrast to noise ratios, than those acquired with SE. The static magnetic field inhomogeneities induced by the compartmentalization of CA are partially refocused using SE but not GRE acquisitions, which results in less signal loss (by approximately a factor of two). Neither sequence is able to refocus the dephasing of protons due to their diffusion through the susceptibility gradients over the duration of the pulse sequence echo time (TE). Simulations and experimental studies aimed at investigating this complex pulse sequence dependency have found that SE measurements are primarily sensitive to the microvasculature ($\sim$10 μm) because their size is similar to the diffusion distance of water during an echo time (Boxerman et al., 1995; Stables et al., 1998; Weisskoff et al., 1994). Consequently, SE based DSC-MRI signals primarily reflect capillary cerebral blood volume (*CBV)* and cerebral blood flow (*CBF)*. GRE measurements exhibit a sensitivity profile that is similar to SE for the microvasculature but then plateaus and remains constant for larger vessels, yielding *CBV* and *CBF* maps that reflect blood vessels of all sizes. As detailed in Section 4.5, the distinct microstructural sensitivity of GRE and SE measures can also be leveraged to estimate mean vessel diameter.

Acquisition strategies for DSC/DCE

Both DSC-MRI and DCE-MRI involve the dynamic acquisition of data before, during, and after injection of an exogenous CA. Despite this parallel, there are several differences with DSC and DCE-MRI that impact the preferred acquisition strategy for each method. One important difference is in selecting an acquisition strategy that is tuned to a specific type of contrast (R_2^* and R_2 in DSC-MRI and R_1 in DCE-MRI). Both methods can be adversely impacted by competing relaxation effects (Boxerman et al., 2006; de Bazelaire et al., 2006; Ewing and Bagher-Ebadian, 2013; Stokes et al., 2016a). Therefore, typical acquisitions for DSC-MRI and DCE-MRI are *intentionally designed* to minimize the influence of competing effects – long TEs and TRs in DSC-MRI minimize T_1 effects, while short TEs and TRs in DCE-MRI minimize T_2^* effects. In addition to acquisition differences, the reported parameters inform on fundamentally different but complementary hemodynamic processes. Thus, the combination of DSC-MRI perfusion and DCE-MRI vascular permeability would provide a significant advantage for fully characterizing various neuropathologies. The acquisition strategies and their advantages and tradeoffs will be discussed in detail below for both DSC-MRI and DCE-MRI, as well as combined DSC-MRI/DCE-MRI. Consensus methods have been previously published (see (Welker et al., 2015) for DSC-MRI and ("DCE MRI Quantification Profile," 2012) for DCE-MRI recommendations) and focus primarily on the minimum basic standards to ensure robust and reproducible results across locations, imaging platforms, and time. While the standardized methods will be presented here briefly for context as traditional options, we will primarily focus on new and promising advanced acquisition strategies, particularly those highlighted in Table 1.

DSC-MRI

Contrast

As described in Section 2.5.3, GRE contrast has higher vessel sensitivity across vessels of all sizes, while SE contrast is maximally sensitive to capillary-sized vessels. As a result, GRE acquisitions have higher contrast to noise ratio (CNR) per dose and tend to be the preferred method clinically. Other advantages of GRE acquisitions are shorter echo times, which enables higher temporal resolution, and the ability to quantify the arterial input function (AIF) when needed. Conversely, for GRE acquisitions, the same susceptibility contrast that provides high vascular sensitivity also causes susceptibility-induced signal dropout in regions with an air-tissue interface. These distortions often preclude the quantification of perfusion parameters in these regions and are a major drawback of GRE acquisitions. While the GRE sensitivity to vessels of all sizes yields higher CNR, it also implies that the perfusion parameters are often dominated by large vessels (so-called large vessel blooming artifact) that overshadow the smaller capillary perfusion signal. As a result, GRE sequences tend to overestimate perfusion due to the impact of macrovascular signal, while SE sequences are more consistent with microvascular perfusion measurements from the reference positron emission tomography (Østergaard et al., 1998a, 1998b). Microvascular deficiencies have been implicated in a number of pathologies (see Applications section), and thus SE acquisitions – with their reduced sensitivity to susceptibility-induced image distortion and specificity to microvasculature – may be advantageous. While traditional single-echo DSC acquisitions require an *a priori* choice between GRE and SE contrast, more advanced methods can acquire both types of contrast within a single sequence to circumvent the individual disadvantages. These sequences have the advantages of providing more information (total and microvascular perfusion, plus vascular characteristics) within a single acquisition and CA dose (Donahue et al., 2000). Fig. 2 demonstrates the use of a combined spin- and gradient-echo (SAGE) sequence (Schmiedeskamp et al., 2013, 2012; Skinner et al., 2014; Stokes et al., 2016a, 2016b) for DSC-MRI. These more advanced pulse sequences will be discussed in more detail in the multi-echo section below.

Pulse sequences: choice of acquisition readout

For DSC-MRI, rapid imaging is required to accurately sample the dynamic contrast-induced MR signal changes. Without adequate temporal resolution, perfusion (specifically, cerebral blood flow) tends to be underestimated (Knutsson et al., 2004). The general consensus, according to the American Society of Functional Neuroradiology (ASFNR), is that a temporal resolution equal to or less than 1.5s is required for DSC-MRI (Welker et al., 2015). Due to the rapid temporal requirements, the most commonly used acquisition strategy for DSC-MRI is single-shot echo planar imaging (EPI). These sequences provide good spatial coverage (typically 15–25 slices for whole brain coverage) with rapid temporal resolution and are widely available on clinical platforms. The main drawbacks to EPI-based acquisitions are signal dropout (particularly around sinuses and, in the case of tumors, around resection cavities) and image distortion. More advanced readout options have been developed to overcome these drawbacks; these options include advanced EPI readouts (Gelderen et al., 2000; Newbould et al., 2007), single-line acquisitions (Quarles et al., 2012), and non-Cartesian readouts such as spiral or radial acquisitions (Jonathan et al., 2013; Paulson et al., 2016). While generally less available clinically, these advanced methods can provide significant advantages over traditional DSC-MRI methods with

Table 1
Recent advances in DSC- and DCE-MRI acquisition methods.

Acquisition	DSC-MRI		DCE-MRI	
	Method	Selected References	Method	Selected References
Readout	PERMEATE	Jochimsen et al., 2007; Newbould et al., 2007	GRASP	Rossi Espagnet et al., 2015
	PRESTO	Gelderen et al., 2000; Pedersen et al., 2004	Dual-temporal resolution	Jelescu et al., 2011
	SPICE	Paulson et al., 2016		
Multi-echo	SAGE	(Schmiedeskamp et al., 2013, 2012; Skinner et al., 2014; Stokes et al., 2014)	Dual-echo	Ewing and Bagher-Ebadian, 2013
	sSAGE	Stokes et al., 2016b; Stokes and Quarles, 2016		
	SPICE	Paulson et al., 2016		
Acceleration	Partial Fourier	d'Arcy et al., 2002; Jonathan et al., 2013 Oesterle et al., 2000	Compressed sensing	Yoon et al., 2014; Smith et al., 2012
	SMS	Eichner et al., 2014 Chakhoyan et al., 2018	MRA + view-sharing	Zhao et al., 2015

single-shot EPI.

A major source of image distortion in single-shot EPI arises from off-resonance effects during the long readouts required to fully sample k-space. One effective method to reduce the readout length is to split the k-space traversal into multiple shots using a segmented or interleaved EPI readout. Because *n*-shots are required to fully sample k-space, segmented EPI often requires reduced repetition times (TRs) to maintain adequate temporal resolution, but this comes at a cost of higher T_1 sensitivity. One example of a novel segmented EPI sequence employs the PRinciples of Echo Shifting with a Train of Observations (PRESTO) to minimize EPI distortion while maintaining image resolution and adequate T_2^* sensitivity (Gelderen et al., 2000; Pedersen et al., 2004). Unlike most MR pulse sequences (wherein TE < TR), the PRESTO sequence employs additional gradients to shift the resulting gradient echo into later TR periods (such that TE > TR). However, one drawback of these time-efficient PRESTO methods is higher T_1 sensitivity due to the shorter TRs (typically less than 20 ms). An alternative multishot EPI method called PERfusion with Multiple Echoes and Temporal Enhancement (PERMEATE) was developed using image acceleration (see section below) to further reduce image distortion and motion sensitivity (Jochimsen et al., 2007; Newbould et al., 2007). The significantly reduced readouts in PERMEATE also permit acquisition of multiple echoes, which provides more accurate R_2^* quantification. This approach can provide multi-echo EPI images with reduced distortion in the same temporal resolution as single-shot EPI and was shown to provide improved quantification of DSC-MRI perfusion parameters (Newbould et al., 2007).

Other alternative readout options are currently under development and may provide advantages over EPI-based readouts. Single-line acquisitions lack the distortions of EPI, but often come at the cost of reduced spatial and temporal resolution and limited flexibility in TEs and TRs. These tend to be more popular options for DCE-MRI, where short TRs and TEs provide an advantage in T_1 sensitivity. Non-Cartesian acquisitions, such as spiral or radial readouts, may provide further benefit over EPI: these acquisitions tend to be more robust to motion, have increased time efficiency, and may permit more aggressive undersampling to improve temporal and/or spatial resolution. One proposed approach is to use a novel hybrid 3D EPI acquisition with radial sampling in-plane (Jonathan et al., 2013). This method – termed 3D RAZIR – permitted acquisition of whole-brain high resolution (1.7 mm isotropic) perfusion data in close agreement with literature values. The drawback to this method is a low native temporal resolution of 10.3s per 3D volume, which was reconstructed to sub-second resolution using a sliding window

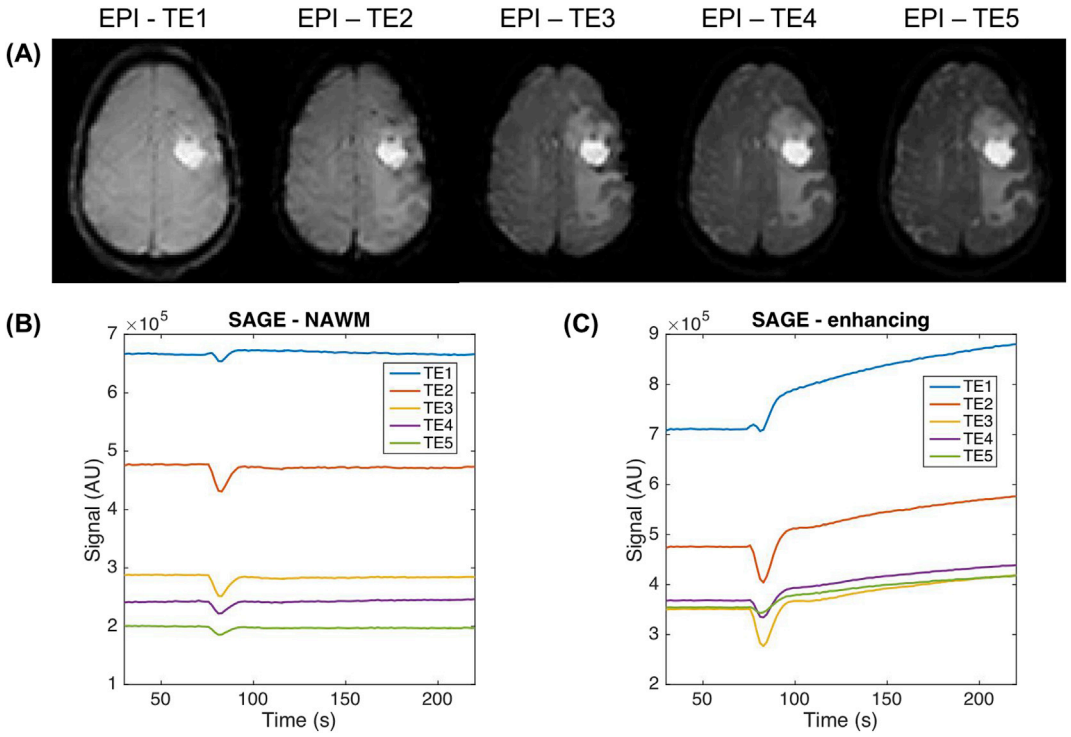

Fig. 2. Representative DSC-MRI data in a recurrent glioblastoma patient. Example EPI images **(A)** and time series using a spin and gradient echo (SAGE) acquisition approach that acquires two GREs (TE1 and TE2), two asymmetric spin echoes (TE3 and TE4) and a SE (TE5). Each echo time yields a dynamic signal time course as shown in normal appearing white matter (NAWM) **(B)** and enhancing **(C)** ROIs. TE1 – TE5 = 8.3, 24, 50, 67, and 83 ms, respectively.

approach (see Acceleration methods, Section 3.1.4). While the low temporal resolution may preclude its use in brain tumor studies, other neuropathologies with less stringent temporal kinetics may benefit from the whole-brain coverage of this approach. Another promising example is the Spiral Perfusion Imaging with Consecutive Echoes (SPICE) method that was used to simultaneously acquire DSC- and DCE-MRI data (Paulson et al., 2016). Using this approach, two echoes with tunable T_1 and T_2^*-weightings, corresponding to short and long TEs, respectively, were acquired with high temporal resolution (Fig. 3). This method is particularly promising as it provides both perfusion and vascular permeability parameters using a single contrast injection with good spatial and temporal resolution. While non-Cartesian options lack the distortions associated with EPI, these methods may induce other types of image artifacts (e.g., spiral-induced blurring) that could impact the resulting perfusion quantification. The other drawbacks for non-Cartesian sampling include limited clinical availability and more complex reconstruction.

Pulse sequences: parameter selection

The chosen TE in GRE DSC-MRI can impact the amount of T_2^*-weighting and image SNR. Longer TEs provide higher T_2^*-weighting but can induce significant signal saturation, particular near large vessels, (Johnson et al., 2004), while shorter TEs result in higher image SNR but also increase sensitivity to T_1 effects (Thilmann et al., 2004). To balance these effects, the typical recommendation for TE is 25–35 ms. Using *rCBV* error minimization as a metric for TE optimization, the optimal TE is equal to a weighted average of the changes in tissue T_2^* during contrast agent passage (Bell et al., 2017a; Boxerman et al., 1997; Thilmann et al., 2004). Due to the bolus-induced signal drop, this is lower than the baseline T_2^*, which is often cited as the preferred TE. While the typical recommendation is acceptable for most applications, the optimal TE for AIF is often shorter due to the reduced T_2^*, and care should be taken with longer TEs to avoid AIF voxels with noise floor or saturation issues. For SE DSC-MRI, the TE is typically longer than GRE acquisitions to permit time for the refocusing pulse.

Compared to conventional single-echo DSC-MRI, advanced multi-echo acquisitions provide several advantages for DSC-MRI, including flexibility in both contrast and TEs. Multi-echo acquisitions can be leveraged to acquire multiple gradient echoes (≥2), single gradient- and spin-echoes, and multiple gradient- and spin-echoes. The simplest of these options is a dual GRE, where an additional short-TE echo is acquired between the excitation pulse and the traditional longer-TE echo. This method also provides more flexibility in the TEs, which may improve characterization of both the AIF (using an optimized shorter TE) and brain tissue (Bell et al., 2017a; Newton et al., 2016). Perhaps more importantly, T_1 leakage effects can be quantified, permitting both direct DCE-MRI analysis and correction of DSC-MRI data for more accurate perfusion analysis (Quarles et al., 2012; Sourbron et al., 2009; Stokes et al., 2016a).

The combination of GRE and SE into the SAGE sequence involves acquisition of two GREs, two asymmetric spin-echoes, and a single SE (Schmiedeskamp et al., 2013, 2012; Skinner et al., 2014; Stokes et al., 2014). The clinically-feasible simplified SAGE (sSAGE) sequence similarly involves acquisition of two GREs and a single SE, trading the asymmetric spin-echoes for a more efficient analysis method and potential for shorter SE TEs (Stokes et al., 2016b; Stokes and Quarles, 2016). These advanced multi-echo SAGE and sSAGE sequences provide a multitude of hemodynamic parameters (Fig. 4 below): both macro- and microvascular perfusion (with additional post-processing for CA leakage effects), vascular permeability, and vessel architectural properties (Schmiedeskamp et al., 2013, 2012; Skinner et al., 2014; Stokes et al., 2016b; Stokes and Quarles, 2016). The ability to inform upon multiple distinct hemodynamic parameters in a single acquisition provides a more complete basis for understanding various neuropathologies.

Repetition time is closely tied to the resulting temporal resolution of the dynamic time-course; with traditional single-shot EPI acquisitions, the repetition time is equivalent to the temporal resolution and is driven by the number of slices and TE. The typical recommendation is a TR less than or equal to 1.5 s. More advanced acquisitions may have shorter repetition times, but at a cost of increased T_1-weighting.

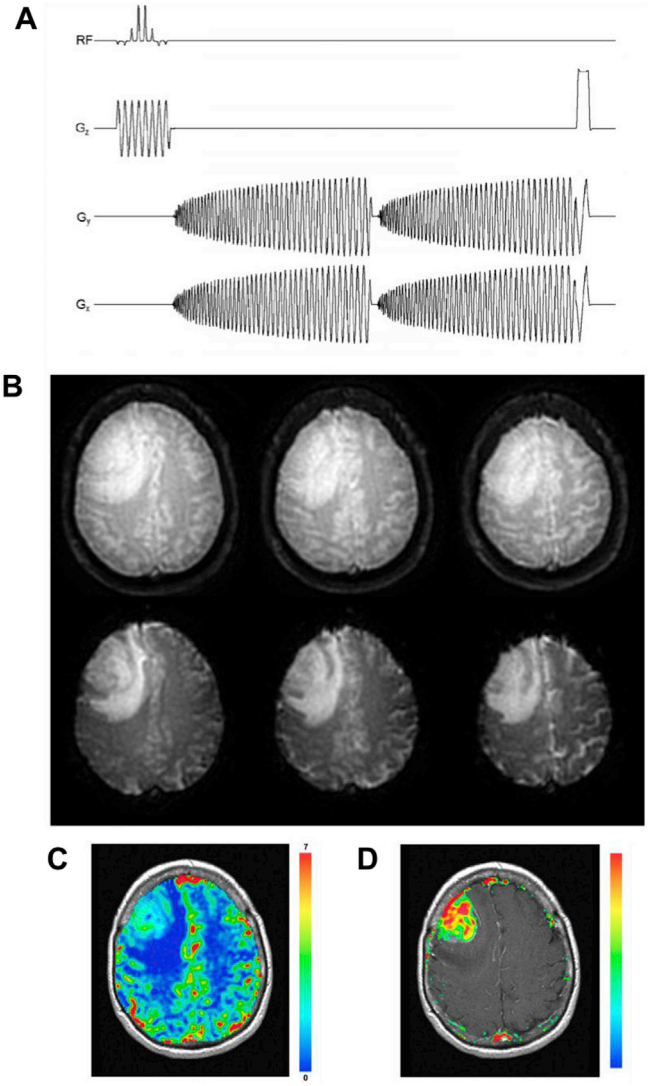

Fig. 3. The SPICE pulse sequence employing dual GRE spiral-out trajectories **(A)**. Multi-slice images from the first and second TE (top and bottom, respectively) **(B)**. Analysis of the acquired DSC-MRI data in a gliobastoma patient yielding maps of *rCBV* ***(C)*** and K^{trans} **(D)**. Figure adapted with permission from (Paulson et al., 2016).

Flip angle recommendations for GRE DSC-MRI are typically between 60 and 70°. Higher flip angles increase the image SNR but induce more T_1-weighting, while lower flip angles lead to lower SNR and reduced *CBF* accuracy (Calamante et al., 2007). For SE DSC-MRI, a flip angle of 90° is generally prescribed.

The minimum recommended requirements for spatial resolution are generally 1–3 mm in-plane and 3–5 mm through-plane, with adequate slice coverage for whole brain imaging. Insufficient spatial resolution leads to partial volume effects (PVEs), particularly in the AIF, and can impact the accuracy of the resulting perfusion metrics (Chen et al., 2005). The trade-off between spatial and temporal resolution may be tuned based on the clinical application, where temporal resolution may be sacrificed for finer spatial resolution or vice versa.

The dynamic scan time is generally determined by the pathology of interest. For brain tumors, the minimum recommendation is 2 min, with the injection occurring at 30–60s to provide an adequate measure of the

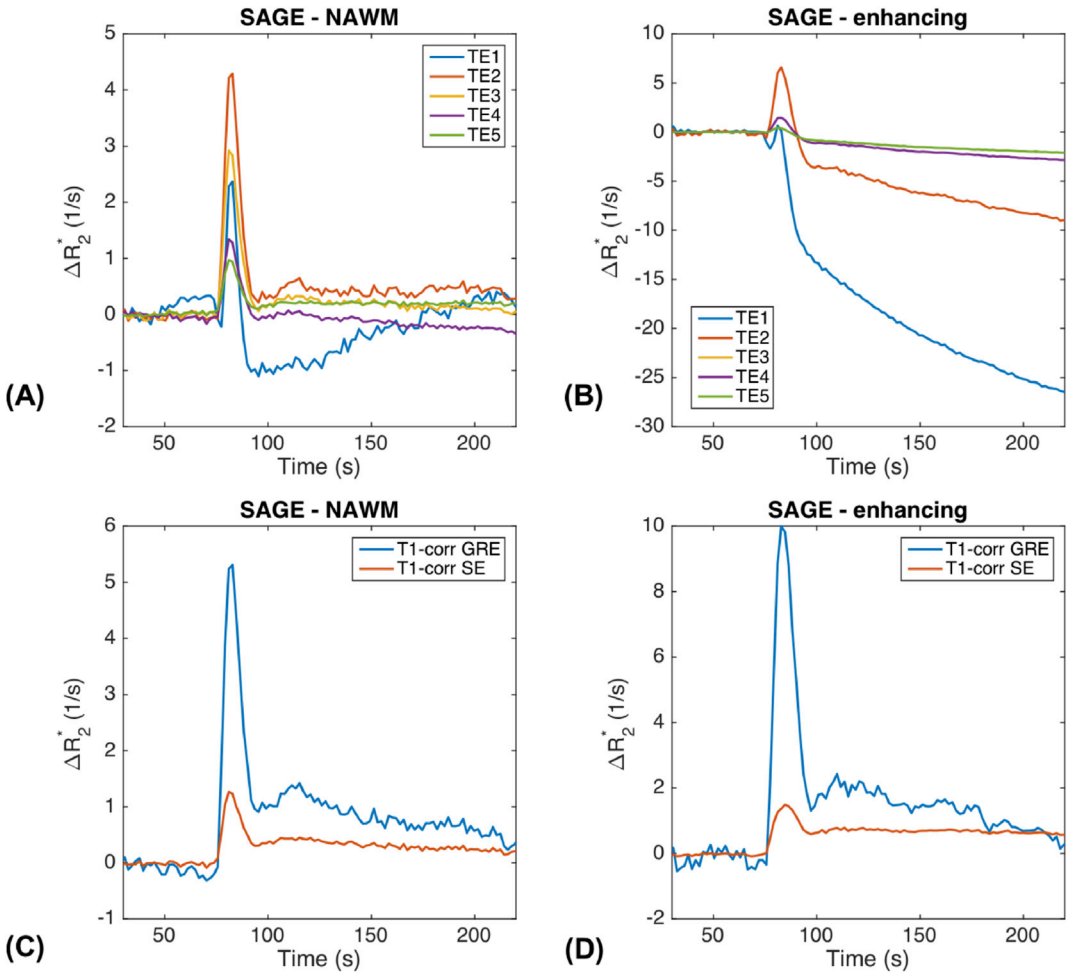

Fig. 4. The spin and gradient echo DSC-MRI signals shown in Fig. 2 were used to compute $R_2^*(t)$ (and $\Delta R_2(t)$) curves for each of the five echoes in NAWM **(A)** and enhancing tumor **(B)** ROIs. Note that the signals for the lower echo times are influenced by T_1 effects (negative $R_2^*(t)$). By leveraging multiple echoes, the ΔR_2^* and ΔR_2 curves can be corrected for T_1 effects as shown in NAWM **(C)** and enhancing tumor **(D)** ROIs. TE1 – TE5 = 8.3, 24, 50, 67, and 83 ms, respectively.

baseline signal intensity. At least 120 points should be acquired, particularly if leakage correction is to be performed, corresponding to 2–3 min for 1–1.5 s temporal resolution (Paulson and Schmainda, 2008). For stroke and other pathologies with significant bolus dispersion and delay, longer dynamic scan times may be required, with similar baseline duration (Calamante et al., 2006). While longer scan durations can emphasize the influence of tracer recirculation, this does not generally impact the resulting perfusion metrics (provided deconvolution is used); on the other hand, truncated scan durations can lead to significant errors in the resulting perfusion metrics (Kosior and Frayne, 2010).

Pulse sequences: acceleration methods

DSC- and DCE-MRI have considerable competing pulse sequence demands to both sample fast (to characterize rapid signal changes) and with high resolution (to resolve anatomical structures). In order to attain adequate temporal and spatial resolution, some form of image acceleration is often required. This is typically achieved with k-space undersampling strategies, though care must be taken to avoid undersampling artifacts. For example, in parallel imaging, additional information from receiver coils is exploited for image reconstruction, either in image-space (SENSitivity Encoding (SENSE)) or k-space (GeneRalized Autocalibrating Partial Parallel Acquisition (GRAPPA)). Using parallel imaging in the PERMEATE method, the reduced acquisition readout was leveraged for improved temporal resolution, acquisition of multiple echoes, and reduced image distortion (Jochimsen et al., 2007; Newbould et al., 2007).

Other methods of undersampling include partial Fourier acquisitions, where high-frequency k-space is undersampled and reconstructed from the remaining k-space, or view-sharing methods, where the undersampled data is reconstructed from other dynamic time-frames. A sliding window view-sharing method, where k-space is split into interleaves and consecutive "windows" are combined for image reconstruction, has been used to improve DSC-MRI temporal resolution (d'Arcy et al., 2002; Jonathan et al., 2013). Keyhole view-sharing techniques have also been proposed for DSC-MRI (Oesterle et al., 2000), where center low-frequency k-space is acquired at each dynamic, while the high-frequency information is obtained from a reference image and is shared among the undersampled dynamic images. The use of compressed sensing to randomly undersample k-space may also provide further image acceleration (Smith et al., 2012).

A promising new method of image acceleration is simultaneous multi-slice (SMS) acquisitions, which leverages multi-band RF pulses to acquire multiple slices simultaneously that are then separated using parallel imaging. SMS was recently shown to improve slice coverage in a gradient- and SE DSC-MRI sequence; in principle, either spatial or temporal resolution could be improved using SMS (Chakhoyan et al., 2018; Eichner et al., 2014).

Dosing recommendations

The vast majority of clinical DSC-MRI studies use gadolinium-based contrast agents, as they tend to be well characterized and widely available. Historically, many studies have used gadopentetate (Gd-DTPA,

trade name Magnevist), which is a linear Gd-based CA. More recent studies have employed macrocyclic Gd-based CAs (such as gadebenate dimeglumine, trade name MultiHance, and gadobutrol, trade name Gadavist) due to their preferable pharmacokinetic properties (Frenzel et al., 2008). High concentration CAs have also been developed, such as Gadavist, which have the advantage of smaller injection volumes and thus tighter bolus profiles. Care must be taken to account for the different relaxivity properties of each CA when converting to CA concentration. The limitations for Gd-based CAs include risks of nephrogenic systemic fibrosis (NSF) in patients with renal insufficiency (Leiner and Kucharczyk, 2009) and concerns about Gd accumulation over time in normal brain regions as a function of dose (Kanda et al., 2015; McDonald et al., 2015).

In clinical applications with BBB breakdown (e.g., brain tumors), there is the potential for significant Gd-based CA extravasation, which severely impacts the accuracy of the resulting perfusion metrics (Boxerman et al., 2006). To minimize the impact of T_1 leakage effects due to extravascular CA, a preload dose of CA can be administered. In addition to clinical indication, a preload may be appropriate in more T_1-weighted sequences (high flip angle, short TR and TE). A recent study in brain tumors with varying preload doses showed diminishing returns for increasing preload doses: while T_1 leakage effects decreased with each preload dose up to 0.1 mmol/kg, T_2^* leakage effects increased with each preload dose up to 0.25 mmol/kg (Bell et al., 2017b). As such, in cases where a preload dose is indicated, a CA preload dose of $\leq$0.1 mmol/kg body weight should be given 5–10 min prior to primary bolus. It should be noted that this preload dose can also be used as the primary injection for DCE-MRI acquisition (see DCE-MRI section).

The primary CA dose in DSC-MRI should balance the need for a significant T_2^* effect (i.e., drop in MR signal intensity) with the potential for signal saturation. For GRE acquisitions, the doses typically range from 0.1 to 0.2 mmol/kg body weight (single- and double-dose, respectively), while for SE acquisitions, higher doses up to 0.3 mmol/kg may be required to induce similar MR signal drops (Hu et al., 2010). The dose should be administered with a power injector at a rate greater than 4 ml/s, followed by a saline flush at the same rate, to produce an adequate bolus profile. Slower injections may lead to underestimated perfusion parameters (van Osch et al., 2003). The injection should be performed in the right arm if possible to prevent CA flux into venous structures.

As an alternative to Gd-based CA, iron-oxide-based agents such as ferumoxytol have been proposed. These agents are known to stay intravascular over the dynamic time frame and permit steady-state CBV mapping (Troprès et al., 2001; Varallyay et al., 2013). In addition, a combined R1 and R2* relaxometry approach was recently developed to obtain ferumoxytol-based CBV without confounding signal-concentration non-linearities (Rivera-Rivera et al., 2018). For DSC-MRI, the recommended dose for ferumoxytol is 3 mg Fe/kg body weight (range: 1–7 mg/kg); this dose should be diluted by a factor of 5 in saline and injected using a power injector at a rate of 1–2 ml/s, followed by a saline flush (20–30 ml) at the same rate (Varallyay et al., 2017). While Fe-based CAs prevent CA leakage effects and may be used in patients with renal insufficiency, they are less well-characterized and may induce hypersensitivity reactions (Toth et al., 2017). In addition, they do not provide same expected enhancement on T_1w post-CA images, necessitating the use of additional injections of Gd-based agents, when identifying regions of BBB disruption is desired (e.g. glioblastoma).

DCE-MRI

Special considerations for DCE-MRI in the brain

DSC-MRI perfusion has been the radiologic mainstay for brain imaging due to the high susceptibility effects induced by BBB sequestration of CA in the vasculature. DCE-MRI is more widely utilized outside the brain, where CA extravasates into the extravascular space to induce significant T_1 relaxation effects. However, it has long been recognized that intracranial neoplasms cause breakdown of the BBB, permitting CA extravasation. It is also increasingly recognized that BBB disruption occurs in cerebrovascular disease (including stroke), normal and pathological aging, and multiple sclerosis. This section will cover the use of DCE-MRI to assess BBB integrity and the unique challenges for DCE-MRI in the brain.

Pulse sequences: T_1 mapping and dynamic data acquisition

The data acquisition in DCE-MRI largely determines the appropriate level of data analysis, which can include qualitative ("curvology"), semi-quantitative, and/or quantitative analysis. Quantitative analysis of DCE-MRI requires knowledge of the CA concentration, which is proportional to the tissue T_1 value. In order to convert the T_1-weighted DCE-MRI signal to dynamic T_1 values, a pre-contrast T_1 map must be acquired. Inversion recovery sequences – the gold standard method for T_1 mapping – are rarely used clinically due to the long acquisition times. More clinically feasible methods for T_1 mapping include Variable Flip Angle (VFA) and Look-Locker (LL). Though these methods are faster, this may come at the expense of accuracy (Stikov et al., 2015). As VFA methods generally overestimate tissue T_1 and LL methods generally underestimate tissue T_1, it may be possible to create site-specific calibration schemes using IR validation (Stikov et al., 2015). In contrast to these voxel-wise T_1 mapping methods, several studies have proposed the use of a fixed predefined T_1 value for conversion to CA concentration (Abe et al., 2015; Haacke et al., 2007). As the spatial distribution of T_1 values can vary significantly, this method has been shown to introduce bias into the resulting DCE-MRI parameters (Tietze et al., 2015b); therefore, voxel-wise T_1 mapping methods are generally recommended.

For the dynamic data acquisition, the temporal requirements for DCE-MRI tend to be less stringent than DSC-MRI, unless an AIF is required, and largely depend on the brain tissue kinetics in the pathology of interest, and to some extent on the chosen analysis method (see Analysis section). While high temporal resolution and T_2^* sensitivity dominate pulse sequence choice in DSC-MRI, DCE-MRI pulse sequences are often optimized to maximize sensitivity to T_1 effects. The vast majority of DCE-MRI studies utilize 3D GRE sequences (including spoiled GRE sequences (SPGR) and ultrafast SPGR variations) (Heye et al., 2014). These sequences provide high T_1-weighting and flexibility in balancing the requisite spatial and temporal resolution. Using a pre-contrast T_1 map, the T_1-weighted signals can be converted to dynamic CA concentration curves for subsequent DCE-MRI analysis.

Similar to DSC-MRI, image acceleration is often used in DCE-MRI to improve spatial and/or temporal resolution. For example, dynamic compressed sensing can be combined with parallel imaging (GRAPPA) and either 3D or 2D + SMS encoding schemes for DCE-MRI, resulting in improved noise characteristics and higher spatiotemporal resolution (Yoon et al., 2014). Another promising method is the golden-angle radial sparse parallel (GRASP) scheme, which employs radial k-space encoding with golden angle ordering to achieve high spatial resolution and flexible *post-hoc* temporal resolution as high as 2.5 s (Rossi Espagnet et al., 2015). As high undersampling factors can induce significant image artifacts, another technique is to combine highly undersampled data (acceleration factors up to 30x) with a constrained reconstruction to improve both spatial resolution (<1 mm in-plane) and provide whole brain coverage (Guo et al., 2016). Time-resolved MR angiography sequences that exploit keyhole view-sharing have also been utilized for DCE-MRI, under multiple vendor-specific acronyms (including TWIST, TRICKS, and 4D-TRAKS). These methods are particularly promising to achieve higher temporal resolution in brain tumor studies (Zhao et al., 2015). As an alternative to image acceleration, dual-temporal resolution protocols have been proposed to achieve high temporal resolution during the first-pass (at the expense of spatial resolution) and high spatial resolution thereafter (with low temporal resolution) (Jelescu et al., 2011).

Rather than measuring a T_1-weighted signal, some studies have

employed quantitative T_1 mapping at each dynamic time point, which may reduce sensitivity to signal instabilities and pulse sequence parameters. As T_1 mapping requires longer acquisition time, several rapid T_1 mapping methods have been developed. These fast T_1-mapping variants are typically based on the LL method and can provide quantitative dynamic T_1 measurements with temporal resolution adequate for certain pathologies. For example, T_1 mapping with partial IR (TAPIR) has been utilized for DCE-MRI in multiple sclerosis and vascular cognitive impairment with a temporal resolution of 3.5 min (Taheri et al., 2011), while TOMROP (T-One by Multiple Read-Out Pulses) has been utilized in a preclinical stroke model (Ewing et al., 2003). Even with these faster T_1 mapping schemes, these methods suffer from relatively poor temporal resolution, which may preclude both some analysis methods and their use in certain neuropathologies.

Pulse sequences: parameter selection

DCE pulse sequence design is primarily driven by need for high T_1-weighting, coupled with balancing temporal and spatial resolution. The chosen set of parameters (TE, TR, and flip angle) influence the level of T_1-weighted and the resulting sensitivity to CA concentration. Specifically, expressions can be derived for both the minimum detectable and maximum measurable CA concentrations (i.e., the detection envelope) (Schabel and Parker, 2008). Typically, TE and TR are minimized for rapid acquisition, with flip angle more flexible for optimization. According to the consensus recommendations, the acceptable limit for pulse sequence parameters are TE up to 2.5 ms and TR up to 7 ms, while the ideal pulse sequence parameters are TE < 1.5 ms, TR < 3 ms ("DCE MRI Quantification Profile," 2012). The recommendation for flip angle is between 25 and 35°.

The balance between spatial and temporal resolution is determined by the pathology. BBB disruption in brain tumors leads to rapid extravasation kinetics, necessitating higher temporal resolution at the expense of spatial resolution. On the other hand, reduced flow is often observed in ischemia, which permits moderate temporal and spatial resolution. Other applications such as aging and multiple sclerosis have slow extravasation, permitting low temporal resolution that can be traded for the necessary high spatial resolution. According to a 2014 meta-analysis of DCE-MRI in the brain, the median temporal resolution was 5.3 s in intracranial neoplasms (30 studies, 716 subjects), 14.0 s in stroke or cerebrovascular disease (11 studies, 482 subjects), 34.8 s in MS (8 studies, 186 subjects), and 229.0 s in Alzheimer's disease (1 study, 30 patients) (Heye et al., 2014). The desired spatial resolution is typically at least 1–2 mm in plane and <5 mm through-plane ("DCE MRI Quantification Profile," 2012).

The total scan time in DCE-MRI is substantially longer than DSC-MRI and is similarly determined by pathology. The scan time also determines the appropriate level of analysis, and short scan durations may preclude quantitative assessment of certain parameters, such as that described in Section 4.7. Relative to other pathologies, brain tumors have the shortest scan duration requirements, while aging and MS have slower extravasation and thus longer scan durations. More specifically, the meta-analysis by Heye et al. found that the median scan duration was 5.5 min for intracranial neoplasms, 9 min for stroke or cerebrovascular disease, 21.8 min in MS, and 34.4 min in Alzheimer's disease (Heye et al., 2014). Reducing the dynamic scan time (or temporal resolution) results in increased parameter uncertainty (Larsson et al., 2013; Vidarsson et al., 2009).

For quantitative analysis of DCE-MRI, an arterial input function (commonly either individual or population-based) is required. To adequately sample the AIF, high temporal resolution is required to accurately sample the CA first-pass. In addition, the AIF has a substantially higher peak CA concentration (often 5–10 mM) compared to the tissue CA concentration (typically 1–2 mm) (Schabel and Parker, 2008). This can lead to an additional challenge in pulse sequence design – optimizing parameters for lower tissue CA concentration sensitivity while not saturating the AIF CA concentration. Another technical challenge for AIF determination in DCE-MRI is the presence of strong T_2^* effects from intravascular CA. These effects can manifest even at the relatively short TEs in DCE-MRI (Ewing and Bagher-Ebadian, 2013). Potential solutions include the use of UTE sequences to minimize the influence of T_2^* effects (Gharagouzloo et al., 2015; Rivera-Rivera et al., 2018) or multi-echo pulse sequences that measure and remove T_2^* effects (Ewing and Bagher-Ebadian, 2013).

Dosing recommendations

DCE-MRI studies employ both linear and macrocyclic Gd-based CAs to induce T_1 effects, with Gd-DTPA being the most commonly used CA (Heye et al., 2014). The advantages and limitations of these agents are discussed above in the DSC-MRI dosing section. Unlike DSC-MRI, iron--oxide based agents are not generally used for DCE-MRI as they remain intravascular over the dynamic time frame. The standard Gd-based CA dose for DCE-MRI is 0.1 mmol/kg body weight; furthermore, no Gd-based CA should be injected in the 24 h prior to DCE-MRI. Similar to DSC-MRI, the injection should be performed using a power injector in the right arm if possible to prevent CA flux into venous structures. The injection rate is lower for DCE-MRI at 2–4 ml/s, followed by saline flush (20–30 ml) at same rate.

Analysis of DSC-MRI and DCE-MRI data

The conventional hemodynamic parameters calculated from DSC-MRI are *CBV*, *CBF* and mean transit time (*MTT)*, while DCE-MRI in the brain is primarily used to estimate the contrast agent volume transfer constant between blood plasma and the extravascular extracellular space (K^{trans}) and the volume fraction of the extravascular extracellular space (v_e). These hemodynamic parameters reflect the process of arterial blood flow (liters of blood per minute) through the capillary system of the brain tissue (grams of tissue), and into the interstitium in the case of DCE-MRI, resulting in units of mL/min/g.

Conversion of MRI signal into concentration curves

The measured MR signals require conversion to contrast agent concentration time profiles prior to kinetic analysis. The approximation of MR signal ($S(t)$) as a function of time for both DSC/DCE, assuming an SPGR sequence, is based on:

$$S(t) = M_0 \frac{\sin(\alpha)[1-\exp(-TR\times R_1(t))]}{1-\cos(\alpha)\exp(-TR\times R_1(t))}\exp\left(-TE\times R_2^*(t)\right) = M_0 \times E_1(t)\times E_2(t) \quad (2)$$

where M_0 is the equilibrium longitudinal magnetization; α is the flip angle; and $R_i(i=1,2)$ is the relevant relaxation rate ($R_i = 1/T_i$). For brevity, $E_i(i=1,2)$ is the term containing either T_1 or T_2^* effects.

Estimating concentration curves in tissue using single echo DSC-MRI

As shown in Eq. (1), the change in CA concentration is assumed to be linearly proportional to the change in transverse relaxation rate, $\Delta R_2^*(t)$, within the tissue, with a proportionality constant that is equal to the contrast agent relaxivity, r_2^* (Kiselev, 2001). In conventional DSC-MRI, r_2^* is not known *a priori* and is often set to unity. By re-arranging Eq. (2), the change in transverse magnetization can be calculated. For a single echo DSC-MRI acquisition:

$$\Delta R_2^*(t) = R_2^*(t) - R_2^*(0) = -\frac{1}{TE}\ln\left[\frac{S(t)}{S(0)}+\frac{E_1(0)}{E_1(t)}\right] \approx -\frac{1}{TE}\ln\left[\frac{S(t)}{S(0)}\right] \quad (3)$$

where $S(0)$ is the baseline signal before CA arrival. Typically, T_1 effects, as notated by the E_1 term, are assumed to be negligible. When this assumption is not valid (i.e., when the BBB breaks down), specialized acquisition methods (described in Sections 3.1.3 and 3.1.5) and/or post-

processing methods (see Section 4.9.2) should be employed. In order to ensure good CNR, $S(0)$ is typically averaged over approximately 60 s worth of pre-contrast time points (Welker et al., 2015).

Estimating concentration curves in tissue using dual echo DSC-MRI

With a dual echo DSC acquisition, contrast agent induced T_1 effects can be removed (Kuperman et al., 1996; Vonken et al., 1999, 2000):

$$\Delta R_2^*(t) = \frac{1}{TE_2 - TE_1} \ln\left[\frac{S_{TE_1}(t)}{S_{TE_2}(t)} \times \frac{S_{TE_1}(0)}{S_{TE_2}(0)}\right] \quad (4)$$

Estimating concentration curves in tissue using SAGE

For SAGE data, there are two primary methods for analysis. The original SAGE analysis (Schmiedeskamp et al., 2013; Skinner et al., 2014) is based on non-linear fitting of all five echoes to derive $R_2(t)$ and $R_2^*(t)$. As the nonlinear fit for SAGE can be time-consuming, the simplified SAGE (sSAGE) analysis uses a simplified acquisition of three echoes and an analytical solution for $\Delta R_2(t)$ and $\Delta R_2^*(t)$ (Stokes et al., 2016b; Stokes and Quarles, 2016). The sSAGE method provides statistically equivalent hemodynamic measures in a clinically efficient manner. The $\Delta R_2^*(t)$ for sSAGE can be obtained using Eq. (4). The signal extrapolated to TE = 0 (see Eq. (7) below) can be used to estimate and remove T_1 effects from $\Delta R_2(t)$:

$$\Delta R_2(t) = \frac{1}{TE_{SE}}\left(\ln\left(\frac{S_{TE_{SE},pre}}{S_{TE_{SE}}(t)}\right) - \ln\left(\frac{S_{TE=0,pre}}{S_{TE=0}(t)}\right)\right) \quad (5)$$

As in the SAGE implementation, the dual-echo $\Delta R_2^*(t)$ and sSAGE $\Delta R_2(t)$ can be used for subsequent DSC-MRI analysis (Section 4.2), while $S_{TE} = 0$ can be used for DCE-MRI analysis (Section 4.7). This simplified acquisition may permit shorter SE TEs, while the analytical computation of T_1-corrected $\Delta R_2^*(t)$ and $\Delta R_2(t)$ was over 450 times faster than the nonlinear fitting method (Stokes et al., 2016b). Representative examples of uncorrected $\Delta R_2^*(t)$ and $\Delta R_2(t)$ and T_1-corrected $\Delta R_2^*(t)$ and $\Delta R_2(t)$ curves are shown in Fig. 4.

Estimating concentration curves in arterial voxels using DSC-MRI

While intravascular T_1 effects are assumed negligible in brain tissue due to the low vascular volume fraction, this is not the case when voxels used to measure the AIF are located within major vessels. The adverse effects of T_1 on AIF estimation and the derived perfusion parameters (Calamante et al., 2007) can be mitigated using dual- or multi-echo acquisitions (Newton et al., 2016). Additionally, it is well established that the assumption of a linear relationship between $\Delta R_2^*(t)$ and contrast agent concentration is not reliable. Instead, a quadratic relationship should be assumed in order to avoid errors in CBF (Calamante et al., 2009).

Estimating concentration curves in tissue using DCE-MRI

In a DCE-MRI acquisition, the change in CA concentration is assumed to be linearly proportional to the change in the longitudinal relaxation rate, ΔR_1. Quantifying $\Delta R_1(t)$ is not as straightforward as the logarithmic approach used in DSC-MRI. The pre-contrast T_{10} values must be first determined by a separate T_1 mapping acquisition before DCE-MRI. Once pre-contrast T_{10} values have been established, T_1 changes over time can be found through derivation of Eq. (2) (Landis et al., 2000):

$$\frac{1}{T_1(t)} = -\frac{1}{TR} ln\left[\frac{1 - \frac{1-exp(-TR/T_1)}{1-cos(\alpha)exp(-TR/T_1)}\frac{S(t)}{S(0)}}{1 - cos(\alpha)\frac{1-exp(-TR/T_1)}{1-cos(\alpha)exp(-TR/T_1)}\frac{S(t)}{S(0)}}\right] \quad (6)$$

Note here that it is assumed that T_2^* effects are negligible (TE $\ll T_2^*$). Equations (2) and (6) can be used to derive the tissue contrast agent concentration, assuming a known contrast agent T_1 relaxivity.

T_1-weighted signal from multi-echo acquisitions

Dual-echo and SAGE acquisitions, in addition to providing $\Delta R_2^*(t)$ curves free from T_1 effects (Eq. (4)), also have the advantage of providing T_1-weighted signals (free from T_2^* effects) by extrapolation to TE = 0 (Vonken et al., 1999):

$$S_{TE=0}(t) = S_{TE_1}(t) \cdot \left(\frac{S_{TE_1}(t)}{S_{TE_2}(t)}\right)^{TE_1/(TE_2-TE_1)} \quad (7)$$

This T_1-weighted signal can be used for DCE-MRI analysis, particularly in multi-echo DSC studies (Paulson et al., 2016; Schmiedeskamp et al., 2013, 2012; Skinner et al., 2014; Stokes et al., 2014; Vonken et al., 1999). For DCE-MRI studies with multiple echoes, removal of T_2^* effects (due to intravascular CA compartmentalization) using Eq. (7) can prevent underestimations of the AIF CA concentration (de Bazelaire et al., 2006; Ewing and Bagher-Ebadian, 2013).

DSC-MRI kinetic modeling

The DSC-MRI hemodynamic parameters are derived from indicator dilution theory (Axel, 1980; Meier and Zierler, 1954). Assuming the CA is compartmentalized within blood vessels, a simple closed, one-compartment model can be applied. The arterial input function, $C_{AIF}(t)$, characterizes the system's input and the residue function, $R(t)$, describes the fraction of contrast agent remaining in the vasculature at time t after injection. Note here that the residue function is always a positive, decreasing function over time with $R(t = 0) = 1$. In a DSC-MRI study, the signal in each voxel reflects the tissue contrast agent concentration, $C_t(t)$, which is related to $C_{AIF}(t)$ and $R(t)$ according to the following convolution equation:

$$C_t(t) = \frac{\rho}{H_f} CBF \int_0^t C_{AIF}(t)R(t-\tau)\, d\tau \quad (8)$$

where ρ is the brain tissue density (typically, 1 g/ml tissue) and H_f is the hematocrit factor (typically, 0.67) which accounts for the difference in hematocrit between the AIF and the capillary system (Rempp et al., 1994). From the MR perfusion dataset, the only two measured concentration time curves are $C_{AIF}(t)$ and $C_t(t)$. The residue function is determined by deconvolving these two measured time curves, and *CBF* (mL of blood/100 g of tissue/min) is determined from the initial height of the residue function, since $R(0) = 1$. Maps of *CBV* (mL of blood/100 g of tissue) can be derived using:

$$CBV = \frac{H_f}{\rho}\frac{\int_{-\infty}^{+\infty} C_{tissue}(t)\ dt}{\int_{-\infty}^{+\infty} C_{AIF}(t)\ dt} \quad (9)$$

Finally, the central volume principle states that the *MTT* (sec) is simply:

$$MTT = \frac{CBV}{CBF} \quad (10)$$

Representative CBV, CBF and MTT maps are illustrated in Fig. 5.

Capillary transit time heterogeneity and the oxygen extraction fraction

While CBV, CBF, and MTT represent the primary biomarkers of interest for the majority of DSC-MRI studies, there is an increased use of advanced kinetic models to estimate sub-voxel transit time heterogeneity and oxygen extraction fraction. The CA bolus can take varying amounts of time to traverse the capillary system depending on its path and velocity, and the resulting distribution of transit times, $h(t)$, can be derived from the residue function using:

$$h(t) = -\frac{dR(t)}{dt} \quad (11)$$

In practice, the CNR of DSC-MRI data is insufficient to enable reliable estimation of $h(t)$ and necessitates the use of a parametric estimation of the residue function. Previous studies have suggested that gamma-variate

modeling of the transit time distribution provides a good estimation of the underlying microvasculature (Jespersen and Ostergaard, 2012; Mouridsen et al., 2014):

$$h(\tau;\alpha,\beta) = \frac{1}{\beta^{\alpha}\Gamma(\alpha)}\tau^{\alpha-1}e^{-\tau/\beta} \quad (12)$$

where α and β are the gamma-variate parameters. With this definition, the MTT can be determined as αβ and the standard deviation of the distribution, typically referred to as the capillary transit time heterogeneity (CTH), is $CTH = \beta\sqrt{\alpha}$. Additionally, a delay parameter, δ, can be added to the model to account for the delay between the AIF and tissue time curves. This model-dependent formulation of $h(t)$, and by extension, $R(t)$, can be substituted into Eq. (8). A representative map of CTH is illustrated in Fig. 5.

It is well established that capillary flow heterogeneity directly influences the efficacy of oxygen extraction, and homogenization of flow patterns can increase oxygen extraction efficacy (Kuschinsky and Paulson, 1992; Ostergaard et al., 2000). Jespersen et al. derived a method to quantify the maximum oxygen extraction fraction (OEF^{max}) by first modeling the oxygen extraction from a single capillary as a function of transit time, $Q(\tau)$, and then integrating over the distribution of transit times as defined in Eq. (13) (Jespersen and Ostergaard, 2012):

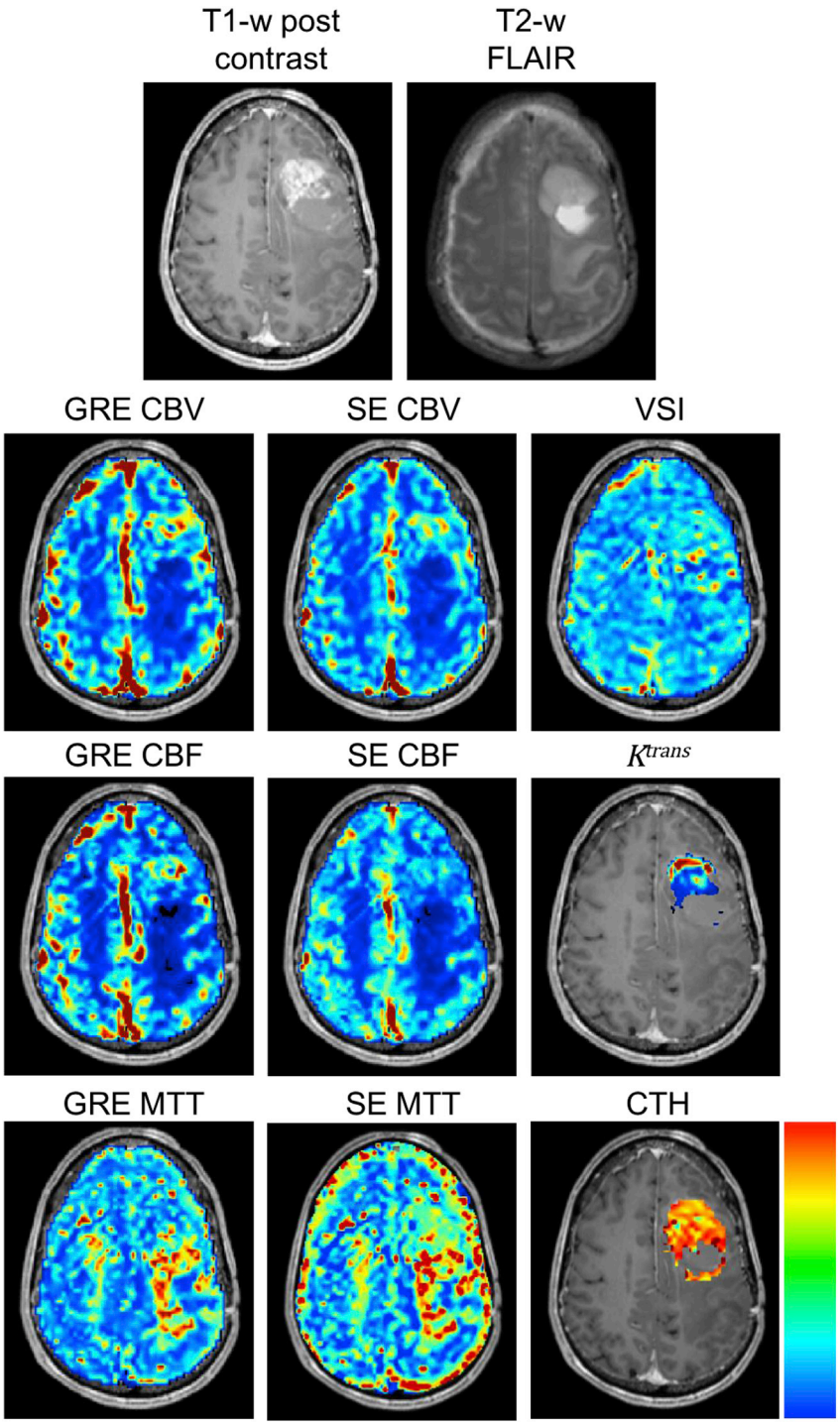

Fig. 5. Example spin and gradient echo (SAGE) based DSC-MRI maps in the glioblastoma patient data highlighted in Figs. 2 and 3 along with the corresponding post-contrast T_1-weighted and fluid-attenuated inversion recovery (FLAIR). As would be expected, the tumor CBV, CBF, MTT and VSI values are higher than those found in contralateral NAWM. Also note the differences between GRE and SE maps within the tumor, particular for CBF and MTT. The K^{trans} and CTH maps also exhibit regional heterogeneity within the tumor. Such differences highlight the unique and complementary nature of multi-echo SAGE hemodynamic and vascular sensitivity. For clarity, relative parameter maps are shown using the illustrated colorbar.

$$OEF^{max} = \int_0^{\infty} h(\tau)Q(\tau)\, d\tau \tag{13}$$

Computing the residue function

Multiple perfusion biomarkers depend on the determination of the residue function from the continuous convolution represented by Eq. (8). Two main approaches exist for deconvolution: model-independent and model-dependent methods. The most commonly used model-independent approach is the singular value decomposition (SVD) method, which was shown to perform better against the early, simple model-dependent approaches (Ostergaard et al., 1996b, 1996a). However, more sophisticated model-dependent approaches, specifically a Bayesian Estimation model, have been developed and are promising especially for advanced DSC-MRI modeling. For these reasons, the SVD method and Bayesian estimation will be covered in the following sections.

Model-independent method: singular value decomposition (SVD)

The SVD approach necessitates two important steps during the deconvolution process: first, discretization of the continuous convolution (Eq. (8)) and second, regularization of the resulting ill-posed inverse problem. Through simulations and patient data, Sourbron et al. rigorously examined the different options for each of these two steps considering the presence of delay and dispersion and implementation into a clinical workflow (Sourbron et al., 2007b, 2007a). Here, we will introduce the discretization and regularization methods most commonly used today along with best practices.

The discrete measurements of the AIF and the tissue time curves are represented as two n-element vectors where n is the number of measurement points: $C_i = C_t(i \cdot \Delta t)$ and $A_i = C_{AIF}(i \cdot \Delta t)$ where $i = 0, \ldots, n-1$. Once discretization is applied, the continuous convolution integral can be written in matrix form (Sourbron et al., 2007b):

$$\mathbf{C} = \mathbf{AR}\Delta t \tag{14}$$

where matrix $\mathbf{C}$ is the tissue concentration time curve, matrix $\mathbf{A}$ is the AIF concentration time curve and is dependent on the chosen discretization method, matrix $\mathbf{R}$ is the residue function, and Δt is the sampling interval. The resulting matrix $\mathbf{R}$ follows the same notation as matrices $\mathbf{C}$ and $\mathbf{A}$, $R_i = R(i \cdot \Delta t)$.

As mentioned, the elements a_{ij} in matrix $\mathbf{A}$ will depend on the discretization method. The complete derivation of matrix $\mathbf{A}$ can be found in (Sourbron et al., 2007b). First, the notation for elements $a_k^{\pm}$ is given as follows and $a_i^{\pm} = a_i^{+} + a_i^{-}$:

$$\begin{aligned} a_i^{-} &= \frac{2a_i + a_{i-1}}{6} \\ a_i^{+} &= \frac{2a_i + a_{i+1}}{6} \end{aligned} \tag{15}$$

Ostergaard et al. first proposed a singular discretization method (Ostergaard et al., 1996a; an extension of this method, the block-circulant method, is a commonly applied discretization method (Wu et al., 2003). Wu et al. proposed the block-circulant method to minimize errors that may arise due to potential delay between the AIF and tissue concentration curves (explained in detail in the following section). First, both matrices $\mathbf{C}$ and $\mathbf{A}$ must be zero-padded to length L, where $L \geq 2n$. Then, matrix $\mathbf{A}$ is as follows for the block-circulant discretization method:

$$\mathbf{A} = \begin{cases} a_{ij} = a_{i-j}^{\pm}, & (0 < i-j \leq n-1) \\ a_{ij} = a_{i-j+2n-1}^{\pm}, & (i-j \leq -n) \\ a_{ij} = 0, & elsewhere \end{cases} \tag{16}$$

The block-circulant method is advantageous as it provides a means to ensure delay-invariance, although ringing artifacts can arise due to the zero-padding. These ringing artifacts can distort the shape of the residue function, which may not be ideal for some advanced modeling techniques (i.e., estimating capillary transit time heterogeneity).

An alternative and promising approach for the AIF discretization is the Volterra method where the matrix $\mathbf{A}$ is defined as follows (Sourbron et al., 2007b):

$$\mathbf{A} = \begin{cases} a_{i0} = a_i^{-}, & (0 < i \leq n-1) \\ a_{ii} = a_0^{+}, & (0 < i \leq n-1) \\ a_{ij} = a_{i-j}^{\pm}, & (1 < i \leq n-1,\ 0 < j < i) \\ a_{ij} = 0, & elsewhere \end{cases} \tag{17}$$

Here the diagonal and first column of matrix $\mathbf{A}$ will be different than that of the block-circulant method (Eq. (16)). It has been shown that this Volterra method provides more accurate perfusion calculations.

After discretization, one must then solve a least-squares problem to find the residue function:

$$\min_{\mathbf{R}} ||\mathbf{AR} - \mathbf{C}_2|| \tag{18}$$

The inverse of matrix $\mathbf{A}$ is typically written by its SVD components:

$$\mathbf{A}^{-1} = \mathbf{V}\, \mathrm{Diag}(1/\sigma_1, 1/\sigma_2, \ldots, 1/\sigma_n)\mathbf{U}^{\mathbf{T}} \tag{19}$$

Matrices $\mathbf{V}$ and $\mathbf{U}^{\mathbf{T}}$ are the orthogonal and transpose orthogonal matrices that contain the singular vectors of $\mathbf{A}$. The diagonal elements are the singular eigenvalues of the matrix. Then the solution for the residue function to the least-squares problem in Eq. (19) is:

$$\mathbf{R} = \mathbf{V}\, \mathrm{Diag}(1/\sigma_1, 1/\sigma_2, \ldots, 1/\sigma_n)\mathbf{U}^{\mathbf{T}}\mathrm{C} \tag{20}$$

This is an ill-posed problem that necessitates regularization to determine both a mathematical and physiological solution. A common approach is the truncated SVD method, which sets eigenvalues to zero below a certain threshold and results in diminished oscillations in the residue function, providing a more physiologically reasonable result. This threshold may either be enforced *a priori* as proposed early on by Ostergaard et al. (recommended to be 20% of the maximum eigenvalue element) (Ostergaard et al., 1996a) or adaptive based on the SNR of the tissue concentration curve (Liu et al., 1999). Both of these means are common in DSC-MRI today. However, alternative methods using a standard-form Tikhonov regularization (SFTR) have been suggested (Sourbron et al., 2007a).

SFTR is another form of regularization that adds an L2-norm of the solution as a quadratic constraint:

$$\min_{\mathbf{R}} \left\{ ||\mathbf{AR} - \mathbf{C}||_2^2 + \mu^2 ||\mathbf{R}||_2^2 \right\} \tag{21}$$

The regularization parameter μ is determined *a priori* and determines the weight of the regularization term. If μ is set too high, the solution will be over-regularized and the residue function may lose all its structure. If μ is set too low, the solution will become under-regularized and the residue function will be dominated by high-frequency oscillations. To determine this regularization parameter, the L-curve criterion (LCC) or generalized cross validation (GCV) methods have been suggested and may produce similar results (Sourbron et al., 2007a).

In summary, the model-independent approach requires the implementation of SVD to calculate the residue function. The SVD approach demands that two decisions are made with regards to the AIF discretization and regularization method. The most widely-implemented combination today utilizes a block-circulant AIF discretization matrix along with a truncated SVD regularization approach. However, more recent publications show promising results for perfusion estimation utilizing a Volterra AIF discretization matrix along with a SFTR regularization approach (Sourbron et al., 2007a).

Model-dependent method: bayesian estimation

Model-dependent methods force specific assumptions about the

underlying microvasculature by modeling the residue function with a specific analytical model. In the simplest form, a decaying exponential equation, representative of a well-mixed, one compartment model, is used to model the residue function and perfusion parameters can be solved for by using a general nonlinear least squared minimization fit. These methods can be sensitive to noise and have been shown to unreliable when compared to model-independent methods, and therefore have not been widely used (Ostergaard et al., 1996b).

In recent years, more complex modeling using Bayesian estimation has shown to be successful for advanced DSC-MRI perfusion calculations such as transit time heterogeneity (Mouridsen et al., 2006). The Bayesian framework utilizes the analytical representation of the transit time distribution (and associated residue function) described in Eq (15). The advantage of a Bayesian model is that it incorporates prior knowledge about all model parameters by embedding them into a posterior distribution defined by Bayes' rule. Mouridsen et al. demonstrated through simulations and in a stroke patient that a Bayesian model resulted in less bias in CBF measurements than when compared to the SVD (singular discretization with an eigenvalue threshold of 20% for regularization) (Mouridsen et al., 2006).

Vessel size imaging

Simultaneous ΔR_2 and ΔR_2^* measures enable the estimation of several vascular features, beyond conventional CBV maps, that can be used to assess abnormal vascular structure (Lemasson et al., 2013). The ratio $\Delta R_2^*/\Delta R_2$ was originally proposed as relative measure of the mean vessel diameter (mVD) in a voxel (Dennie et al., 1998). Conversely, Jensen et al. demonstrated that the index, Q, is a sensitive marker of microvascular density but not vessel size (Jensen and Chandra, 2000):

$$Q = \frac{\Delta R_2}{\Delta R_2^{*2/3}} \tag{22}$$

Finally, quantitative measures of the vessel size index, VSI, can be computed using (Tropes et al., 2001):

$$VSI = 0.425\left(\frac{ADC}{\gamma \Delta\chi B_o}\right)^{1/2}\left(\frac{\Delta R_2^*}{\Delta R_2}\right)^{3/2}, \tag{23}$$

where ADC is the apparent diffusion coefficient, typically averaged over three directions with a diffusion weighted imaging pulse sequence, γ is the gyromagnetic ratio of the protons, $\Delta\chi$ is the increased susceptibility difference between blood and the surrounding tissue due to the presence of contrast agent, and B_o is the magnetic field strength. In practice, $\Delta\chi$ is measured *in vitro* (Tropes et al., 2001) or estimated *in vivo* by assuming a blood volume fraction in normal tissue (Lemasson et al., 2013; Tropres et al., 2004). A representative map of VSI is illustrated in Fig. 5.

With Gd-based contrast agents, the peak $\Delta R_2(t)$ and $\Delta R_2^*(t)$ values are used for estimating these vascular parameters since the underlying theory assumes high $\Delta\chi$ values. With iron-oxide nanoparticles steady-state data can be used since they induce a substantially higher $\Delta\chi$. In a pre-clinical validation study comparing VSI, Q and mVD with similar parameters derived from histology, VSI provided the highest correlation with histology but all parameters were positively correlated (Lemasson et al., 2013). The quantification, validation and translational challenges of absolute vessel size and microvascular density measures have been previously reviewed (Troprès et al., 2015). In the context of human breast cancer xenografts, a comparison of DSC-MRI and quantitative microCT data revealed that there was no difference between the predictive accuracy of absolute and relative indices of microvascular morphology. This finding highlights the potential clinical value of relative metrics, which could be more amenable to widespread clinical use as they are more easily acquired and computed (Kim et al., 2013).

Vessel architectural imaging

VAI parameters are derived from simultaneously acquired (either single or multi-echo) ΔR_2 and ΔR_2^* curves. As summarized in Section 4.9.2 leakage correction is applied, as necessary, to remove the effects of contrast agent extravasation. The curves are fit to a gamma variate function and area normalized to a reference tissue. The vortex curves are generated by plotting $\Delta R_2^*(t)$ versus $\Delta R_2(t)$. A number of parameters are then used to characterize the voxel-wise vortex curves. First, vortex direction is determined by identifying which time profile peaks first. If ΔR_2^* peaks prior to ΔR_2 the vortex direction is clockwise and vice versa. A linear fit can be used to determine the length of the principal axis (from the origin to the vortex apex) and its magnitude is related to blood volume. The slope of the principal axis can also be computed. Finally, using a best fit approach, the area of the vortex is computed and can be normalized by the length of the long axis to account for variations in blood volume fraction. Several physiologic parameters influence these vortex parameters and their biophysical basis is still under investigation (Digernes et al., 2017). Fig. 6 shows example VAI based vortex curves along with representative parameters in a glioblastoma patient.

DCE-MRI kinetic modeling

The most conventional quantitative analysis of DCE-MRI data relies upon a pharmacokinetic, two-compartment model, that consists of blood plasma volume fraction (v_p) and the extravascular extracellular space (EES) volume fraction (v_e). After the CA is injected into the blood stream it can reversibly diffuse into the EES with rate constants that reflect the contrast agent's influx and efflux across the vascular endothelium. Building off the kinetic models developed by Kety (1951), the DCE-MRI community adopted the following formalism to describe the contrast agent concentration in the tissue, $C_t(t)$, (Tofts et al., 1999):

$$C_t(t) = K^{trans}\int_0^t C_p(t)\exp\big(-k_{ep}(T-t)\big)dt \tag{24}$$

where $C_p(t)$ is the concentration of agent in blood plasma, K^{trans} is the volume transfer constant between blood plasma and the EES and $k_{ep} = K^{trans}/v_e$. A formal derivation of Eq. (24), which is often termed the Tofts model, is presented elsewhere (Yankeelov and Gore, 2009). Note that $C_p(t)$ is not the voxel-wise vascular concentration but is taken to be the AIF, thus assuming that the vascular contribution to $C_t(t)$ is negligible. To account for tissues with high vascular volume fractions, the term $v_pC_p(t)$ can be added to the right side of Eq. (24), and is typically termed the extended Tofts model. Two compartment models that account for both arterial delivery and potentially dispersed or unique voxel-wise vascular concentration profiles have been described (Brix et al., 2004, 1999). Such models enable the characterization of both regional blood flow and the vascular permeability. For an in-depth of description of the many types of compartmental models applied to DCE-MRI data the reader is referred to this review (Sourbron and Buckley, 2012). After a model has been selected, a nonlinear least squares fit is used to estimate the corresponding kinetic parameters. A representative map of K^{trans} is illustrated in Fig. 5.

The heterogeneity of contrast profiles in disease and its impact on the suitability of applying a single DCE-MRI model to every voxel is well-appreciated. For example, the application of the Tofts model to voxels in the brain that exhibit no contrast agent extravasation would lead to spurious kinetic parameter estimates. This has spurred the development of nested-modeling strategies that attempt to identify the most appropriate, and simplest, model for a given characteristic concentration profile (Chwang et al., 2014; Dehkordi et al., 2017; Ewing and Bagher-Ebadian, 2013). The statistical F-test is used to determine whether models of increasing complexity improve curve fitting. In brain tumor patients, three versions of the extended Tofts model, representing

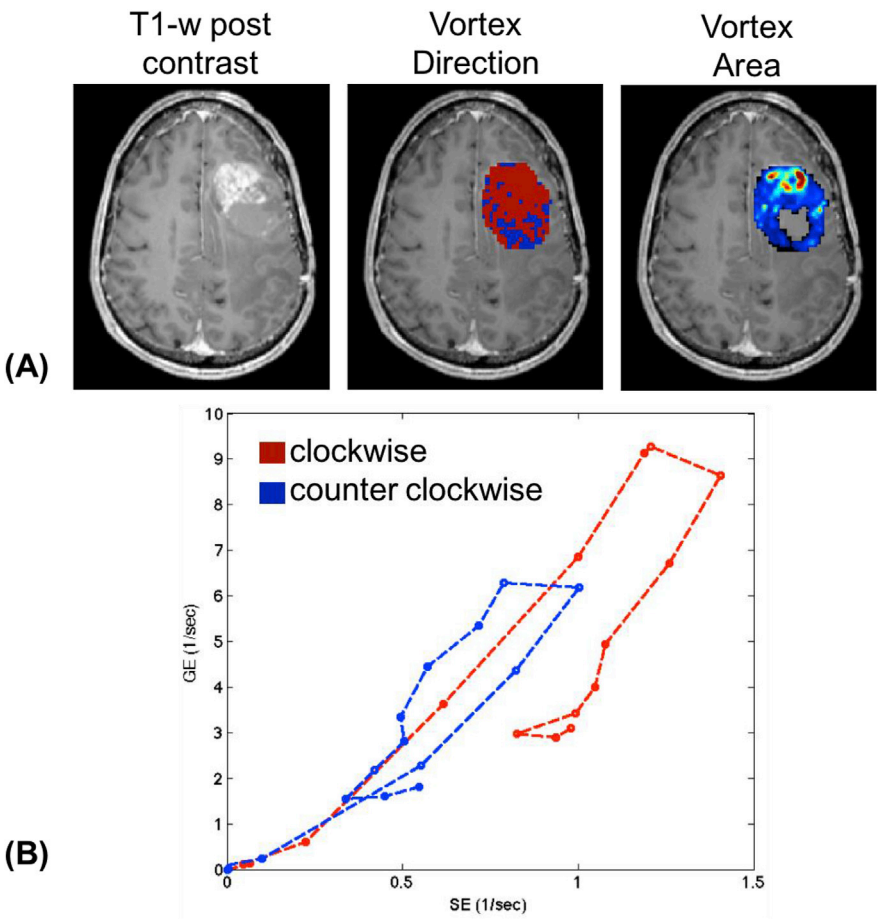

Fig. 6. : Vessel architectural imaging parameters derived from the same recurrent glioblastoma patient data shown in Fig. 2–4. Post-contrast T_1 weighted image and vessel vortex direction and vortex area maps are shown in row **(A)** and example vortex plots for the two directions are plotted in **(B)**. In this patient, the majority of voxels (77%) exhibited a clockwise vortex direction, which reflects a normal vascular architectural phenotype (Emblem et al., 2013). Vortex area maps were highly dissimilar from any of the parameter plots in Fig. 4, potentially highlighting their unique sensitivity.

tissues with 1) no contrast leakage, 2) unidirectional leakage and 3) bidirectional leakage, have been found to sufficiently fit the full range of DCE-MRI data encountered across normal and tumor bearing tissue.

Relative versus absolute quantification

Based on the initial assumptions outlined above, it is already noticeable that achieving absolute quantification is difficult. Typically, the hematocrit and proton density constants in Eq. (8) are assumed to be of literature values or often ignored (set to unity) during post-processing. However, it is known that these factors can vary among patients, different diseases, and differently during treatment response (Metry et al., 1999; Ostergaard et al., 1996a). Furthermore, in DSC experiments the contrast agent relaxivity is unknown and, as mentioned, set to unity. In addition, potential issues with arterial abnormalities and BBB breakdown may affect the signal time curves further confounding absolute quantification. For these reasons, relative parameters are more commonly reported. In DSC-MRI, relative quantification of perfusion parameters is normalized to reference regions, typically contralateral normal appearing white matter (NAWM).

Semi-quantitative perfusion parameters have also shown to be useful for both DSC and DCE acquisitions and do not require pharmacokinetic modeling. Common parameters for assessing stroke disease are time-to-maximum (T_{max}), time-to-peak (*TTP*) and initial area under the curve (*iAUC*) (Calamante et al., 2010; Evelhoch, 1999; Sobesky et al., 2004). For DSC MRI, percent signal recovery (*PSR*) has also shown utility in differentiate of brain tumor types (Mangla et al., 2011).

Potential issues affecting quantification

Several factors may confound quantification of perfusion parameters during both DSC- and DCE-MRI analysis. When these factors are neglected, a scaling error is typically introduced into the perfusion estimations conflating clinical decision-making.

AIF considerations

One of the leading sources of error in quantifying perfusion is the direct result of the determination of the AIF during analysis, specifically where and how the AIF is determined. Where the AIF is determined is dictated by its location relative to the tissue concentration curve, and can either be classified as a global or regional AIF. The most common method uses a global AIF, typically located in the middle branch of the cerebral artery (MCA), which implies that a single AIF measurement is used voxel-wise over the entire brain. A global AIF can be straightforward to define; however, it is not the true input function to the linear time-invariant system used for modeling. Consequently, AIF delay and dispersion may occur and has been shown to introduce substantial errors in CBF and *MTT* (Calamante, 2013; Calamante et al., 2006; Ferreira et al., 2010; Wu et al., 2003). Delay is defined as the delay in arrival time between the AIF and tissue concentration curve, whereas dispersion is the consequence of the contrast bolus becoming dispersed over time. In general, delay effects can easily be accounted for when the deconvolution is computed either by the SVD (i.e. – by choosing AIF discretization methods that have been shown to be insensitive to delay such as both methods described in this review) or Bayesian (i.e. – by incorporating a delay parameter into the

posterior distribution used during modeling). On the contrary, dispersion effects are not that simple to account for when a global AIF is used. Dispersion effects may be mitigated by introducing a vasculature model, however additional errors can easily arise in model-dependent analysis. Instead, implementing multiple regional AIFs, typically located in small branched arteries, during analysis might be a better solution especially for stroke patients where severe dispersion occurs due to stenosis and occlusions (Willats et al., 2011). Recent publications show promising results when applying a novel cerebral vascular model based on fluid dynamics to the branching arteries to compute multiple regional AIFs (Nejad-Davarani et al., 2017a, 2017b).

How the AIF is determined refers to the method used to locate the AIF. Typically, the global AIF is manually selected in (or in voxels adjacent to) either the internal carotid artery or the middle cerebral artery; despite being a simple method, it can be time consuming and user-dependent rendering the process non-reproducible. Furthermore, when local AIFs are warranted, such in stroke patients, a manual selection of multiple local AIFs is unreasonable. Much work has been done to robustly determine the AIF using computer algorithms such as Monte Carlo blind estimation or clustering algorithms (Fluckiger et al., 2010; Schabel et al., 2010; Shi et al., 2014). Although these automatic algorithms improve quantitative perfusion analysis for a single-site, single measurement time-point study, variations in AIF determination methods across multicenter sites may still result in variability with analysis (Huang et al., 2016). For DCE-MRI analysis, variations in AIF methods across 9 imaging sites caused higher variations in K^{trans} and v_e, however, k_{ep} was shown to be less sensitive to variations in AIF. Their results suggest that a fixed AIF determination method and/or k_{ep} might be more ideal for multicenter clinical trials, and for longitudinal multicenter clinical trials the percent changes, instead of absolute values, in parameters should be reported.

BBB breakdown

CA extravasation creates both T_1 and T_2^* leakage effects (as described in Section 2.5.2) which is problematic for analysis since the pharmacokinetic modeling assumes that the CA remains intravascular. These leakage effects can artificially increase (due to T_1 effects) or decrease (due to T_2^* effects) post-contrast DSC signal intensity time curves, and the degree of influence depends on the pulse sequence parameters, preload dose, CA kinetics, and the underlying tissue microstructure (Bell et al., 2017b; Leu et al., 2016; Quarles et al., 2009; Semmineh et al., 2015). During post-processing, these leakage effects are mitigated by applying a model-based leakage-correction algorithm (Bjornerud et al., 2011; Boxerman et al., 2006; Donahue et al., 2000; Leu et al., 2016; Quarles et al., 2005; Stokes et al., 2016a). The most commonly used, and recommended leakage-correction strategy, is to employ contrast agent preload dosing and the Boxerman-Schmainda-Weisskoff (BSW) approach, which assumes unidirectional CA efflux and uses DSC-MRI curves from a "whole-brain non-enhancing" region to estimate and remove the T_1- or T_2^*-based leakage effects from the data measured within the tumor (Boxerman et al., 2006). To avoid the use of preloads, dual-echo and multi-echo acquisitions are currently being evaluated in patients as described in Section 3.1.3. Since these methods eliminate T_1 effects, the acquired data only requires correction of T_2^* leakage effects (Stokes et al., 2016a). The relative magnitude of T_1 and T_2^* leakage effects depends on the pulse sequence parameters and dosing schemes used to collect the data, which, in turn, influences the success of post-processing-based leakage correction. Given the difficulty of comparing the accuracy of different acquisition and post-processing methods in an individual patient, recent efforts have turned to simulations (Leu et al., 2016) and the development of patient data driven digital reference objects (DRO) (Semmineh et al., 2017) in order to identify the optimal DSC-MRI acquisition and analysis protocols. To date, these efforts reveal that the most accurate and precise approach for DSC-MRI at 3 T, when using the recent ASFNR recommendations (Welker et al., 2015). Requires the use of a full dose preload and a full dose bolus injection.

Applications of DSC- and DCE-MRI

For over two decades investigators have leveraged DSC- and DCE-MRI to non-invasively interrogate vascular structure, function and integrity of neurologic disorders, stroke and brain tumors. Conventional DSC- and DCE-MRI are increasingly employed in clinical trials in order to assess early, and more specific, response to therapy. In this section, we will limit our representative examples to advanced applications, specifically those using updated pulse sequences and expanded biophysical and kinetic models that enable the derivation of novel biomarkers of cerebral structure and function. Table 2 summarizes the recommended use of conventional DSC- and DCE-MRI methodology across a range of neuropathologies, potential challenges that need to be considered and advanced hemodynamic metrics that are under investigation.

Brain tumors

DSC-MRI in brain tumors

In the context of brain tumors, DSC-MRI based measures of *CBV* reliably detect the abnormal vascular characteristics exhibited in glioblastoma (Aronen et al., 1994; Donahue et al., 2000; Hakyemez et al., 2005; Schmainda et al., 2004), exhibit high sensitivity to treatment induced changes (Boxerman et al., 2017; Fuss et al., 2001; Schmainda et al., 2015b; Weber et al., 2004) and are highly repeatable (Prah et al., 2015).

Recent efforts have sought to leverage the sensitivity of SE and GRE acquisitions to vessel microstructure and function as well as the insensitivity of multi-echo acquisitions to confounding T_1 effects. As described in Sections 2.5.3 and 4.6 (and illustrated in Fig. 2), VAI relies on characterizing temporal shifts in $\Delta R_2(t)$ and $\Delta R_2^*(t)$ data in order to detect disease related changes in vascular hemodynamics, oxygen saturation and vessel morphology. Emblem et al. recently acquired serial VAI data in recurrent glioblastoma patients receiving anti-angiogenic therapy with cediranib (Emblem et al., 2013). Of the VAI parameters, the vortex direction was best able to differentiate between responding and non-responding patients and predict progression free survival, as illustrated in Fig. 7. In responding patients, the fraction of tumor voxels with a clockwise vortex direction increased with therapy, whereas non-responders exhibited a decrease.

As would be expected, unregulated tumor angiogenesis gives rise to sub-voxel capillary transit time and flow heterogeneity due to, for example, increased vessel tortuosity, regional edema, shunts and thrombosis. DSC-MRI studies of CTH in brain tumors, such as that shown in Fig. 4, confirm this heterogeneity (Ostergaard et al., 2013; Quarles and Schmainda, 2007) (Ostergaard et al., 2013; Quarles and Schmainda,

Table 2
General recommendations and challenges for DSC- and DCE-MRI in various neuropathologies.

	Neuro-oncology	Stroke	Aging	Multiple Sclerosis
DSC and DCE Acquisition	High temporal resolution	Moderate temporal resolution	Low temporal resolution	Low temporal resolution
	Low spatial resolution	Moderate spatial resolution	High spatial resolution	High spatial resolution
Potential pitfalls	CA leakage effects	CA delay	Diffuse pathology	Focal and diffuse characteristics
		AIF identification	Long scan times	Long scan durations
DSC and DCE Parameters (Basic)	rCBV	MTT and Tmax	rCBV	rCBF and rCBV
	Ktrans	Ktrans	Ktrans	Ktrans
DSC and DCE Parameters (Advanced)	VAI CTH Water exchange	OEFmax CTH	VAI CTH	Temporal and spatial patterns of perfusion and BBB permeability

2007; Tietze et al., 2015a). Anti-angiogenic therapy has also been shown to normalize transit time heterogeneity in murine gliosarcoma models (Quarles and Schmainda, 2007). Recently, the potential of CTH, quantified as the standard deviation of the transit time distribution, to predict tumor grade was evaluated (Tietze et al., 2015a). The combination of CTH and CBV data provided the best delineation of tumor grade (AUC = 0.88), as compared to CBV alone (AUC = 0.78).

DCE-MRI in brain tumors

DCE-MRI provides a quantitative assessment of the breakdown of the BBB that accompanies most aggressive brain tumors. Similar to the use of DSC-MRI, kinetic parameters from DCE-MRI differentiate between tumor types (e.g. low versus high grade glioblastoma and primary central nervous system lymphoma) (Abe et al., 2015; Li et al., 2015), prognostication (Dehkordi et al., 2017) and prediction of molecular status (Choi et al., 2017).

A recently developed strategy for DCE-MRI holds the potential to radically shift its structural sensitivity into the realm of metabolic neuroimaging (Rooney et al., 2015). This approach relies on detecting water exchange across cellular membranes. The rate of water exchange has been shown to be proportional to plasma membrane Na^+,K^+- ATPase turnover, hypothesized to be due to active transmembrane water cycling (Rooney et al., 2015; Springer et al., 2014). Though not covered herein the influence of water exchange on DCE-MRI measurements is well-established and acquisition and analysis strategies have been developed to quantify such effects (Bains et al., 2010; Landis et al., 2000; Lee and Springer, 2003). In glioblastoma patients, the water exchange rates were significantly diminished and is postulated as a potential marker of tumor hypoxia. If validated, this reported new application of DCE-MRI would provide a clinically practical approach to identify abnormal tumor metabolism.

Acute stroke

DSC-MRI in acute stroke

Perfusion imaging, with either MRI or CT, continues to be heavily utilized in the context of acute stroke imaging, with the primary goal of identifying patients who are candidates for intravenous tissue plasminogen activator (tPA) or endovascular therapy in order to restore blood flow. Automated analysis tools, such as RAPID, are available and are being used in clinical trials (Albers et al., 2017; Lansberg et al., 2011). A recent meta-analysis, that included 994 patients with perfusion-based treatment and 1819 without perfusion, found that perfusion imaging improves the identification of patients who will benefit from combined intravenous tPA and endovascular thrombectomy. Using this approach patients had nearly twice the probability of achieving independent functional status at 3 months as those without perfusion scans (Ryu et al., 2016).

Given the importance of both perfusion and oxygen extraction on identifying the ischemic penumbra there is an increased interest in using advanced kinetic modeling of DSC-MRI data to derive markers of flow heterogeneity and OEF^{max}. In a cohort of seven patients with anterior circulation strokes, model-dependent (Section 4.4.2) and model-independent (SVD) algorithms were used to compute conventional DSC-MRI perfusion metrics as well as CTH and OEF^{max} (Mouridsen et al., 2014). Final infarct volumes were determined using T_2 FLAIR follow up images that were acquired 1 week to 1 month after the perfusion study. As illustrated in Fig. 8, the MTT, CTH and OEF^{max} maps, determined with model-dependent methods, were best able to regionally predict the final infarct location and volume.

DCE-MRI in acute stroke

Acute ischemic stroke may disrupt the BBB and is generally considered a poor prognostic indicator as it may lead to edema and hemorrhagic transformation (Sandoval and Witt, 2008). DCE-MRI was recently used to characterize the temporal evolution of BBB status after acute ischemic stroke in 42 patients that did not undergo hemorrhagic transformation (Merali et al., 2017). Prolonged BBB disruption (>48 h) was detected in all patients and the vascular permeability was highest in the acute phase (6–48 h) as compared to hyperacute (<6 h) and the subacute (>48 h). The sensitivity of DCE-MRI to BBB degeneration, such as seen in this study, makes it valuable tool with which to select patients for and monitor treatments that attempt to stabilize the BBB.

Aging

Diseases of aging are often associated with deleterious vascular changes, including impaired cerebral microvasculature and increased BBB permeability. In Alzheimer's disease (AD) and other forms of dementia, these changes are thought to be contributing factors in the pathological cascade that leads to cognitive decline.

DSC-MRI in aging

Cerebral hypoperfusion occurs early in the AD trajectory, preceding both structural brain changes and clinical symptoms (Binnewijzend et al., 2016; Bozzao et al., 2001; Chao et al., 2010; Johnson et al., 2005; Maas

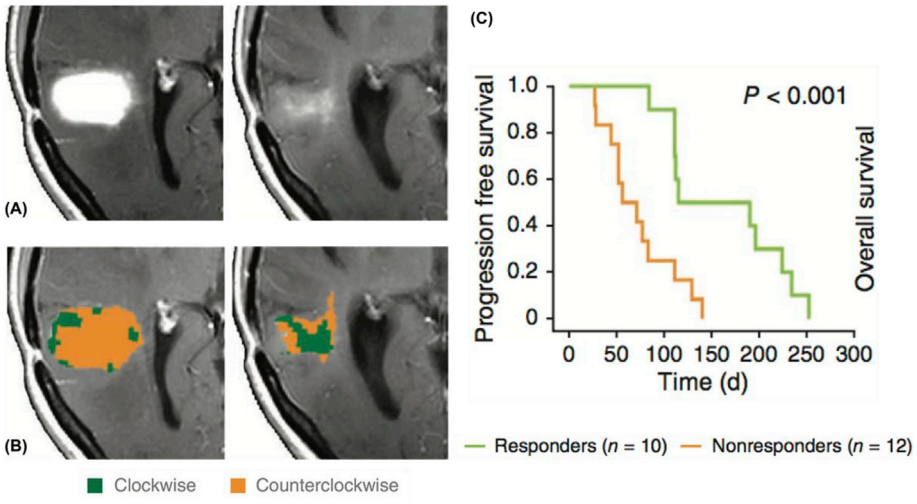

Fig. 7. Assessment of anti-angiogenic therapy in recurrent glioblastoma patients using vessel architectural imaging. Post-contrast T_1- weighted images **(A)** and maps of vortex direction **(B)** before (left) and 28 days after (right) therapy onset. **(C)** Progression free survival curves in responding (median = 153 days) and non-responding patients (median = 64 days) that were identified based on vortex direction. Figure adapted with permission from (Emblem et al., 2013).

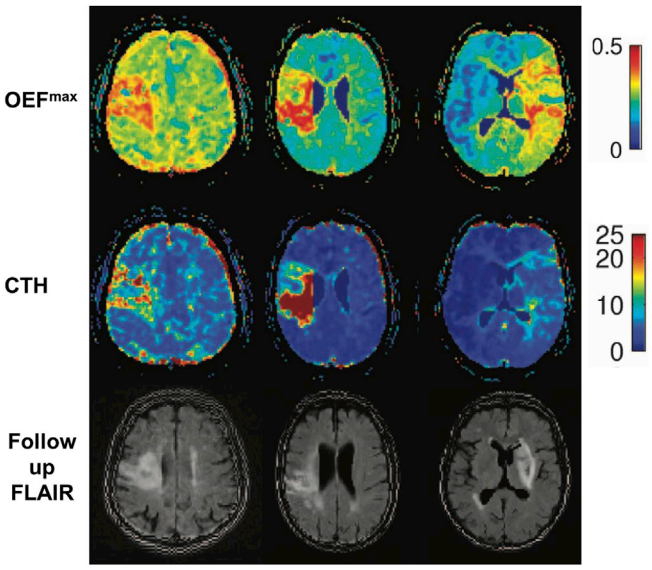

Fig. 8. Example perfusion data acquired in stroke patients, including oxygen extraction fraction (OEF^{max}, unitless) and capillary transit time heterogeneity (CTH, sec) maps and a follow up T2 FLAIR image acquired 1 week–1 month after the perfusion images. Note the strong agreement, in terms of location and size, between the perfusion markers and the final infarct volume depicted on the FLAIR images. Figure adapted with permission from (Mouridsen et al., 2014).

et al., 1997; Mattia et al., 2003). While hypoperfusion can be measured using standard DSC-MRI, advanced DSC-MRI methods may extend our understanding of cerebrovascular age-related changes and provide more sensitive biomarkers of pathology-specific vascular changes. Two advanced biomarkers obtained from DSC-MRI will be discussed here – microvessel density and capillary transit time heterogeneity (CTH).

AD is associated with changes in the vascular architecture, including the density and morphology of cerebral blood vessels. Microvessel density can be assessed using the relaxation shift index Q from GRE and SE acquisitions (Tropes et al., 2001; Wu et al., 2004). In a preclinical study by Ielacqua et al. (2015), DSC-MRI was performed with an iron-oxide CA, and the Q -index was obtained from high-resolution maps of ΔR_2^* and ΔR_2 ($Q \equiv \Delta R_2/(\Delta R_2^*)^{2/3}$). The Q -index was validated as a biomarker of microvessel density (using histopathological CD31 vessel staining) and was found to be decreased in a transgenic amyloid mouse model compared to control mice (Ielacqua et al., 2015). This method could be a novel biomarker for amyloid-related microvascular changes and could be acquired clinically using a multi-echo DSC-MRI study.

In addition to alterations in microvessel density, the capillary morphology is also altered in the development of AD. Cerebral metabolism is impacted by both CBF and the capillary transit time heterogeneity (CTH) (Østergaard et al., 2013). Capillary dysfunction limits the maximum achievable O_2 extraction fraction and could contribute significantly to AD pathology. CTH can be assessed using advanced DSC-MRI methods (Section 4.3) (Mouridsen et al., 2014). Using sequential GRE and SE DSC-MRI, Nielsen et al. (2017) found that hypoperfusion (reduced CBF and CBV) and concomitant elevated MTT and CTH were associated with declines in cognitive function and regional brain atrophy (Nielsen et al., 2017). A strong negative correlation was found between changes over six months in subjects brief cognitive status examination and their change CTH. Relative CTH (= CTH/MTT) has also been shown to correlate with both white matter hyperintensities and symptom severity (Eskildsen et al., 2017). Overall, metrics that incorporate capillary flow information may provide additional prognostic information on cerebral microcirculatory insufficiencies in AD.

DCE-MRI in aging

In addition to microvascular architectural changes, AD pathology has been associated with increases in BBB permeability (Farrall and Wardlaw, 2009; Wang et al., 2006). Using DCE-MRI, several studies have demonstrated regional variations in BBB disruption that are consistent with known AD-vulnerable regions. In one study, BBB permeability was elevated in the hippocampus – a region critical to learning and memory – in patients with mild cognitive impairment compared to healthy controls, while the cerebellum was not impacted (Wang et al., 2006). BBB permeability has been shown to increase with normal aging, with further increases observed in patients with AD (Farrall and Wardlaw, 2009). Conversely, another study demonstrated that BBB permeability may not be a global brain phenomenon in patients with AD, with no significant vascular permeability differences between AD patients and healthy controls across several white and gray matter regions (though altered temporal kinetics were observed) (Starr et al., 2009).

Given the subtle CA extravasation in the aging brain, even in AD pathology, the DCE-MRI protocol for assessing BBB disruption must be adapted for high sensitivity and prolonged time-scales. Using an advanced high-resolution (both spatial and temporal) DCE-MRI protocol, Montagne recently showed that BBB disruption occurs in the hippocampus early in AD pathogenesis and may be implicated in AD-related cognitive decline (Montagne et al., 2015). Haar et al. (2016) utilized a dual-time resolution DCE-MRI consisting of fast and slow pulse sequences to characterize both initial vascular arrival and slower CA tissue extravasation/wash-out, respectively (Haar et al., 2016). Using this method, they found significantly higher BBB permeability in early AD patients than normal controls in multiple brain regions and that this elevated BBB permeability was associated with poorer cognitive test scores. Overall, these advanced methods may permit more sensitive assessment of BBB permeability associated with normal and pathological aging processes.

Multiple sclerosis (MS)

Multiple sclerosis (MS) is characterized by neuroinflammation, demyelination, gliosis, axonal degeneration, and neuronal loss (Trapp and Nave, 2008). Although the precise mechanism of MS is unknown, vascular inflammation is known to play a critical role in the early pathogenesis (Bester et al., 2015; Gaitan et al., 2011; Ge et al., 2005; Wuerfel et al., 2004). Chronic widespread neuro-inflammation is consistently accompanied by hemodynamic changes, and ongoing inflammation in active MS lesions leads to BBB disruption.

DSC-MRI in MS

Numerous studies have shown both increased and decreased locoregional perfusion across the brain in patients with MS, reflecting the complex spatiotemporal dynamics of MS disease progression. More specifically, standard DSC-MRI has been used to demonstrate both normal-appearing white matter (NAWM) hypoperfusion (Ge et al., 2005; Inglese et al., 2008; Sowa et al., 2015) and hyperperfusion (Bester et al., 2015), where the latter may indicate imminent focal WM lesion formation. GM perfusion is also modulated by MS pathology, with deep GM and cortical lesions showing reduced perfusion compared to NAGM (Inglese et al., 2007; Peruzzo et al., 2013). Recent studies have suggested that reduced perfusion is indicative of persistent low-grade inflammation, metabolic or vascular dysfunction, neuronal loss, or even primary ischemia; increased perfusion may indicate a high-inflammatory phase or increased metabolic activity. Moreover, unlike conventional MRI, regional perfusion changes have been found to correlate with clinical disability (Adhya et al., 2006; Bester et al., 2015) and neuropsychological dysfunction (Francis et al., 2013; Inglese et al., 2008, 2007). Overall, these studies suggest that DSC-MRI biomarkers may ultimately play a critical role in revealing the underlying pathophysiology and etiology of MS.

DCE-MRI in MS

One of the hallmark radiological indicators for MS is the formation of

contrast-enhancing lesions, which are observed on T_1-weighted imaging. By exploiting the dynamic nature of contrast enhancement, DCE-MRI may be able to better characterize the spatiotemporal enhancements patterns in active inflammatory MS lesions. Several advanced imaging acquisitions have been developed to increase the sensitivity to BBB permeability occurring over long time-frame. Several studies have developed acquisitions with varying temporal resolution to characterize both the rapid perfusion and slow extravasation kinetics (Jelescu et al., 2011; Larsson et al., 1990). Rapid T_1-mapping for DCE-MRI using TAPIR (Section 3.2.2) was shown to be highly sensitive to subtle BBB vascular permeability (Taheri et al., 2011). Another advanced method demonstrated simultaneous characterization of perfusion and BBB permeability using a combination of view-sharing and parallel imaging to improve both spatial and temporal resolution (Ingrisch et al., 2012). Given the importance of the enhancement pattern, advanced DCE-MRI analysis has been implemented to characterize enhancement heterogeneity parameters, including magnitude, rate, shape (ring-like or nodular), and dynamics (centrifugal or centripetal) (Gaitan et al., 2011; Shinohara et al., 2011). By optimizing both the pulse sequence parameters and analysis model, Cramer and Larsson (2014) showed that long scan durations (>15 min) and high temporal resolution (1.25 s) provided sufficient sensitivity to characterize BBB permeability as low as 0.1 mL/100 g/min (Cramer and Larsson, 2014). Overall, these advanced DCE-MRI acquisitions and analysis methods may provide a more complete picture of the complex neuropathological processes associated with inflammatory phases of MS.

Outlook

In general, the most exciting acquisition-related advances on the frontier of DSC- and DCE-MRI are the use of multiple echo acquisitions, improved k-space sampling strategies, and the use of multi-band to improve spatial and/or temporal resolution. The motivations behind the development of these advanced acquisitions are to provide improved estimation of hemodynamic parameters and to obtain new physiologically-relevant parameters. For example, multi-echo SAGE sequences provide both macro- and microvascular perfusion (with correction for CA leakage effects), vascular permeability, and vessel architectural properties (Schmiedeskamp et al., 2013, 2012; Skinner et al., 2014; Stokes et al., 2016b; Stokes and Quarles, 2016). Given the importance of MR angiography (MRA) and venography in many applications (such as stroke), the development of novel multi-echo sequences with strategic parameter selection could enable the simultaneous derivation of both MRA and perfusion-based vascular parameters (Chen et al., 2018b, 2018a; Ye et al., 2013). Recent developments in k-space sampling strategies include the use of non-Cartesian sampling strategies, such as spiral (Paulson et al., 2016; Schmainda et al., 2015a) and radial (Jonathan et al., 2013; Rossi Espagnet et al., 2015) trajectories, to circumvent the known image distortion and signal artifacts associated with EPI trajectories. Additionally, the ability to combine acceleration strategies (such as parallel imaging, partial Fourier techniques, compressed sensing, and view-sharing) has the potential to significantly improve the spatial and/or temporal resolution. Similarly, the implementation of multiband represents a unique opportunity to improve both spatial and temporal resolution with minimal SNR penalty and similar parameter estimation (Chakhoyan et al., 2018; Eichner et al., 2014). The challenges remaining for clinical adoption of these advanced pulse sequences includes the implementation and standardization of these acquisitions across MR platforms and the development of FDA-approved analysis tools to generate the numerous relevant hemodynamic parameters.

Over the past decade, MR Fingerprinting has emerged as a highly promising, quantitative imaging strategy to simultaneously characterize multiple MR relaxation properties of tissue (e.g. T_1, T_2). In order to accomplish this, a dictionary of "fingerprints" is developed by computationally modeling the MR signal evolution across a range of parameters (e.g. TR, flip angle). Such data is then matched to *in vivo* MRI data, acquired with the same parameters, in order to identify the voxel-wise relaxation properties. Recently, this strategy has been modified for application to steady-state susceptibility-contrast agent based MRI data acquired with multi-gradient and spin echo data, an approach termed MR vascular fingerprinting (Christen et al., 2014; Lemasson et al., 2016). As proposed, it provides measures of blood volume, vessel size and blood oxygenation. This unique approach represents a major shift in how vascular parameters can be quantified since it involves biophysical modeling of the underlying tissue-specific susceptibility-based contrast mechanisms, multi-echo pulse sequences and correlation, rather than kinetic analysis for parameter estimation. This approach has yet to be extended to serial acquisitions during CA passage, like that acquired with SAGE, but a similar strategy could be developed and potentially provide a more comprehensive characterization of tissue microstructure and function (e.g. quantitative measures of vascular tortuosity, vascular phenotyping, oxygen extraction) than is achievable with traditional kinetic analysis. The integration of temporal fingerprinting with SAGE would require the generation of sophisticated biophysical models of MR contrast mechanisms with heterogeneous vascular architecture and CA kinetics (Semmineh et al., 2014), but could provide new opportunities for biomarker development.

For conventional DSC-MRI metrics (e.g. CBV, CBF) the field has sufficiently matured to enable standardization of acquisition and post-processing methods. For DCE-MRI, such consensus recommendations already exist ("DCE MRI Quantification Profile," 2012). While the ASFNR recommendations provide guidelines for DSC-MRI acquisition and dosing protocols in brain tumors (Welker et al., 2015), there has yet to be a consensus protocol on how to analyze this data nor has there been multi-site trials to validate their clinical utility, similar to the evaluation of RAPID software in acute stroke (Lansberg et al., 2011; Warach et al., 2016). Given the challenges of optimizing these protocols over all parameter space in clinical cohorts, digital reference objects have been developed for broad-scale parameter testing and may ultimately drive protocol development (Bosca and Jackson, 2016; Semmineh et al., 2017; Zhu et al., 2015).

To begin to address this limitation, members of the National Cancer Institute's Quantitative Imaging Network (QIN) recently performed a multi-site, multi-platform analyses (7 sites, 20 different analysis methods) of a shared database of DSC-MRI data in low- and high-grade patients (Schmainda et al., 2018). This analysis revealed excellent cross-site and cross-platform agreement with more than 90% of entries exhibiting concordance correlation coefficients greater than 0.8. This analysis confirms that multi-site consistency is a clinically viable goal and could be further enhanced through adoption of common analysis algorithms. In addition to cross-site protocol uniformity, there remains a need in the field for the identification of automated analysis tools that reduce interpatient and inter-study variability. The application of image standardization, which is an approach that translates imaging data to a consistent scale, to DSC-MRI measures of rCBV has been shown to increase repeatability in glioma patients (Prah et al., 2015). The development, validation, and wide spread adoption of such automated analysis tools could greatly facilitate the continued incorporation of DSC- and DCE-MRI into clinical practice.

Across a range of pathologies, contrast enhanced MRI methods have a strong track record of providing valuable and actionable clinic readouts that support their increased use in clinical practice and in the context of clinical trials. The maturation of these methods is the product of continued investigative efforts into their biophysical basis, optimized acquisition strategies, and automated and rigorous analysis algorithms. As highlighted in this article, there remains enormous developmental potential on each of these fronts that will only serve to further advance the clinical integration of DSC-MRI and DCE-MRI.

Grant support

This work was supported by NIH/NCI R01 CA158079, NIH/NCI R01 CA213158, NIH/NCI R01 CA221938, the Arizona Biomedical Research Commission (ADHS16-162414) and the Barrow Neurological Foundation.

References

Abe, T., Mizobuchi, Y., Nakajima, K., Otomi, Y., Irahara, S., Obama, Y., Majigsuren, M., Khashbat, D., Kageji, T., Nagahiro, S., Harada, M., 2015. Diagnosis of brain tumors using dynamic contrast-enhanced perfusion imaging with a short acquisition time. Springerplus 4, 88. https://doi.org/10.1186/s40064-015-0861-6.

Adhya, S., Johnson, G., Herbert, J., Jaggi, H., Babb, J.S., Grossman, R.I., Inglese, M., 2006. Pattern of hemodynamic impairment in multiple sclerosis: dynamic susceptibility contrast perfusion MR imaging at 3.0 T. Neuroimage 33, 1029–1035. https://doi.org/10.1016/j.neuroimage.2006.08.008.

Aime, S., Fasano, M., Terreno, E., 1998. Lanthanide(III) chelates for NMR biomedical applications. Chem. Soc. Rev. 27, 19. https://doi.org/10.1039/a827019z.

Albers, G.W., Lansberg, M.G., Kemp, S., Tsai, J.P., Lavori, P., Christensen, S., Mlynash, M., Kim, S., Hamilton, S., Yeatts, S.D., Palesch, Y., Bammer, R., Broderick, J., Marks, M.P., 2017. A multicenter randomized controlled trial of endovascular therapy following imaging evaluation for ischemic stroke (DEFUSE 3). Int. J. Stroke 12, 896–905. https://doi.org/10.1177/1747493017701147.

Aronen, H.J., Gazit, I.E., Louis, D.N., Buchbinder, B.R., Pardo, F.S., Weisskoff, R.M., Harsh, G.R., Cosgrove, G.R., Halpern, E.F., Hochberg, F.H., 1994. Cerebral blood volume maps of gliomas: comparison with tumor grade and histologic findings. Radiology 191, 41–51. https://doi.org/10.1148/radiology.191.18134596.

Axel, L., 1980. Cerebral blood flow determination by rapid-sequence computed tomography: theoretical analysis. Radiology 137, 679–686.

Bains, L.J., McGrath, D.M., Naish, J.H., Cheung, S., Watson, Y., Taylor, M., Ben Logue, J.P., Parker, G.J.M., Waterton, J.C., Buckley, D.L., 2010. Tracer kinetic analysis of dynamic contrast-enhanced MRI and CT bladder cancer data: a preliminary comparison to assess the magnitude of water exchange effects. Magn. Reson. Med. 64, 595–603.

Bell, L.C., Does, M.D., Stokes, A.M., Baxter, L.C., Schmainda, K.M., Dueck, A.C., Quarles, C.C., 2017a. Optimization of DSC MRI echo times for CBV measurements using error analysis in a pilot study of high-grade gliomas. AJNR Am. J. Neuroradiol. 38, 1710–1715. https://doi.org/10.3174/ajnr.A5295.

Bell, L.C., Hu, L.S., Stokes, A.M., McGee, S.C., Baxter, L.C., Quarles, C.C., 2017b. Characterizing the influence of preload dosing on percent signal recovery (PSR) and cerebral blood volume (CBV) measurements in a patient population with high-grade glioma using dynamic susceptibility contrast MRI. Tomography 3, 89–95. https://doi.org/10.18383/j.tom.2017.00004.

Belorizky, E., Fries, P.H., Helm, L., Kowalewski, J., Kruk, D., Sharp, R.R., Westlund, P.-O., 2008. Comparison of different methods for calculating the paramagnetic relaxation enhancement of nuclear spins as a function of the magnetic field. J. Chem. Phys 128, 052315. https://doi.org/10.1063/1.2833957.

Bester, M., Forkert, N.D., Stellmann, J.P., Sturner, K., Aly, L., Drabik, A., Young, K.L., Heesen, C., Fiehler, J., Siemonsen, S., 2015. Increased perfusion in normal appearing white matter in high inflammatory multiple sclerosis patients. PLoS One 10, e0119356. https://doi.org/10.1371/journal.pone.0119356.

Binnewijzend, M.A., Benedictus, M.R., Kuijer, J.P., van der Flier, W.M., Teunissen, C.E., Prins, N.D., Wattjes, M.P., van Berckel, B.N., Scheltens, P., Barkhof, F., 2016. Cerebral perfusion in the predementia stages of Alzheimer's disease. Eur. Radiol. 26, 506–514. https://doi.org/10.1007/s00330-015-3834-9.

Bjørnerud, A., Johansson, L.O., Briley-Saebø, K., Ahlström, H.K., 2002. Assessment of T_1 and T^*2 effects in vivo and ex vivo using iron oxide nanoparticles in steady state-dependence on blood volume and water exchange. Magn. Reson. Med. 47, 461–471. https://doi.org/10.1002/mrm.10066.

Bjornerud, A., Sorensen, A.G., Mouridsen, K., Emblem, K.E., 2011. T1- and T2*-dominant extravasation correction in DSC-MRI: part I–theoretical considerations and implications for assessment of tumor hemodynamic properties. J. Cereb. Blood Flow. Metab. 31, 2041–2053. https://doi.org/10.1038/jcbfm.2011.52.

Bloembergen, N., Morgan, L.O., 1961. Proton relaxation times in paramagnetic solutions. Effects of electron spin relaxation. J. Chem. Phys. 34, 842–850. https://doi.org/10.1063/1.1731684.

Bosca, R.J., Jackson, E.F., 2016. Creating an anthropomorphic digital MR phantom–an extensible tool for comparing and evaluating quantitative imaging algorithms. Phys. Med. Biol. 61, 974–982. https://doi.org/10.1088/0031-9155/61/2/974.

Boxerman, J.L., Ellingson, B.M., Jeyapalan, S., Elinzano, H., Harris, R.J., Rogg, J.M., Pope, W.B., Safran, H., 2017. Longitudinal DSC-MRI for distinguishing tumor recurrence from pseudoprogression in patients with a high-grade glioma. Am. J. Clin. Oncol. 40, 228–234. https://doi.org/10.1097/COC.0000000000000156.

Boxerman, J.L., Hamberg, L.M., Rosen, B.R., Weisskoff, R.M., 1995. MR contrast due to intravascular magnetic susceptibility perturbations. Magn. Reson. Med. 34, 555–566. https://doi.org/10.1002/mrm.1910340412.

Boxerman, J.L., Prah, D.E., Paulson, E.S., Machan, J.T., Bedekar, D., Schmainda, K.M., 2012. The Role of preload and leakage correction in gadolinium-based cerebral blood volume estimation determined by comparison with MION as a criterion standard. AJNR Am. J. Neuroradiol. 33, 1081–1087. https://doi.org/10.3174/ajnr.A2934.

Boxerman, J.L., Rosen, B.R., Weisskoff, R.M., 1997. Signal-to-noise analysis of cerebral blood volume maps from dynamic NMR imaging studies. J. Magn. Reson. Imaging 7, 528–537. https://doi.org/10.1002/jmri.1880070313.

Boxerman, J.L., Schmainda, K.M., Weisskoff, R.M., 2006. Relative cerebral blood volume maps corrected for contrast agent extravasation significantly correlate with glioma tumor grade, whereas uncorrected maps do not. Am. J. Neuroradiol. 27, 859–867.

Bozzao, A., Floris, R., Baviera, M.E., Apruzzese, A., Simonetti, G., 2001. Diffusion and perfusion MR imaging in cases of Alzheimer's disease: correlations with cortical atrophy and lesion load. Am. J. Neuroradiol. 22, 1030–1036.

Brix, G., Bahner, M.L., Hoffmann, U., Horvath, A., Schreiber, W., 1999. Regional blood flow, capillary permeability, and compartmental volumes: measurement with dynamic CT—initial experience. Radiology 210, 269–276. https://doi.org/10.1148/radiology.210.1.r99ja46269.

Brix, G., Kiessling, F., Lucht, R., Darai, S., Wasser, K., Delorme, S., Griebel, J., 2004. Microcirculation and microvasculature in breast tumors: pharmacokinetic analysis of dynamic MR image series. Magn. Reson. Med. 52, 420–429. https://doi.org/10.1002/mrm.20161.

Calamante, F., 2013. Arterial input function in perfusion MRI: a comprehensive review. Prog. Nucl. Magn. Reson. Spectrosc. 74, 1–32.

Calamante, F., Christensen, S., Desmond, P.M., Østergaard, L., Davis, S.M., Connelly, A., 2010. The physiological significance of the time-to-maximum (Tmax) parameter in perfusion MRI. Stroke 41, 1169–1174. https://doi.org/10.1161/STROKEAHA.110.580670.

Calamante, F., Connelly, A., Van Osch, M.J.P., 2009. Nonlinear $\Delta R\ 2$ * effects in perfusion quantification using bolus-tracking MRI. Magn. Reson. Med. 61, 486–492. https://doi.org/10.1002/mrm.21839.

Calamante, F., Vonken, E.J., van Osch, M.J., 2007. Contrast agent concentration measurements affecting quantification of bolus-tracking perfusion MRI. Magn. Reson. Med. 58, 544–553. https://doi.org/10.1002/mrm.21362.

Calamante, F., Willats, L., Gadian, D.G., Connelly, A., 2006. Bolus delay and dispersion in perfusion MRI: implications for tissue predictor models in stroke. Magn. Reson. Med. 55, 1180–1185. https://doi.org/10.1002/mrm.20873.

Caravan, P., Ellison, J.J., McMurry, T.J., Lauffer, R.B., 1999. Gadolinium(III) chelates as MRI contrast agents: structure, dynamics, and applications. Chem. Rev. 99, 2293–2352. https://doi.org/10.1021/cr980440x.

Chakhoyan, A., Leu, K., Pope, W.B., Cloughesy, T., Ellingson, B., 2018. Improved spatiotemporal resolution of dynamic susceptibility contrast perfusion MRI in brain tumors using simultaneous multi-slice echo-planar imaging. Am. J. Neuroradiol. 39, 43–45.

Chao, L.L., Buckley, S.T., Kornak, J., Schuff, N., Madison, C., Yaffe, K., Miller, B.L., Kramer, J.H., Weiner, M.W., 2010. ASL perfusion MRI predicts cognitive decline and conversion from MCI to dementia. Alzheimer Dis. Assoc. Disord. 24, 19–27. https://doi.org/10.1097/WAD.0b013e3181b4f736.

Chen, J.J., Smith, M.R., Frayne, R., 2005. The impact of partial-volume effects in dynamic susceptibility contrast magnetic resonance perfusion imaging. J. Magn. Reson Imaging 22, 390–399. https://doi.org/10.1002/jmri.20393.

Chen, Y., Liu, S., Buch, S., Hu, J., Kang, Y., Haacke, E.M., 2018a. An interleaved sequence for simultaneous magnetic resonance angiography (MRA), susceptibility weighted imaging (SWI) and quantitative susceptibility mapping (QSM). Magn. Reson. Imaging 47, 1–6. https://doi.org/10.1016/j.mri.2017.11.005.

Chen, Y., Liu, S., Wang, Y., Kang, Y., Haacke, E.M., 2018b. STrategically Acquired Gradient Echo (STAGE) imaging, part I: creating enhanced T1 contrast and standardized susceptibility weighted imaging and quantitative susceptibility mapping. Magn. Reson. Imaging 46, 130–139. https://doi.org/10.1016/j.mri.2017.10.005.

Choi, Y.S., Ahn, S.S., Lee, H.-J., Chang, J.H., Kang, S.-G., Kim, E.-H., Kim, S.H., Lee, S.-K., 2017. The initial area under the curve derived from dynamic contrast-enhanced MRI improves prognosis prediction in glioblastoma with unmethylated MGMT promoter. Am. J. Neuroradiol.

Christen, T., Pannetier, N.A., Ni, W.W., Qiu, D., Moseley, M.E., Schuff, N., Zaharchuk, G., 2014. MR vascular fingerprinting: a new approach to compute cerebral blood volume, mean vessel radius, and oxygenation maps in the human brain. Neuroimage 89, 262–270. https://doi.org/10.1016/j.neuroimage.2013.11.052.

Chwang, W.B., Jain, R., Bagher-Ebadian, H., Nejad-Davarani, S.P., Iskander, A.S.M., VanSlooten, A., Schultz, L., Arbab, A.S., Ewing, J.R., 2014. Measurement of rat brain tumor kinetics using an intravascular MR contrast agent and DCE-MRI nested model selection. J. Magn. Reson. Imaging 40, 1223–1229. https://doi.org/10.1002/jmri.24469.

Corot, C., Robert, P., Idée, J.M., Port, M., 2006. Recent advances in iron oxide nanocrystal technology for medical imaging. Adv. Drug Deliv. Rev. https://doi.org/10.1016/j.addr.2006.09.013.

Cramer, S.P., Larsson, H.B., 2014. Accurate determination of blood-brain barrier permeability using dynamic contrast-enhanced T1-weighted MRI: a simulation and in vivo study on healthy subjects and multiple sclerosis patients. J. Cereb. Blood Flow. Metab. 34, 1655–1665. https://doi.org/10.1038/jcbfm.2014.126.

d'Arcy, J.A., Collins, D.J., Rowland, I.J., Padhani, A.R., Leach, M.O., 2002. Applications of sliding window reconstruction with cartesian sampling for dynamic contrast enhanced MRI. Nmr Biomed. 15, 174–183.

DCE MRI Quantification Profile, 2012. Quant. Imaging Biomarkers Alliance.

de Bazelaire, C., Rofsky, N.M., Duhamel, G., Zhang, J., Michaelson, M.D., George, D., Alsop, D.C., 2006. Combined T2* and T1 measurements for improved perfusion and permeability studies in high field using dynamic contrast enhancement. Eur. Radiol. 16, 2083–2091. https://doi.org/10.1007/s00330-006-0198-1.

De Leōn-Rodríguez, L.M., Martins, A.F., Pinho, M.C., Rofsky, N.M., Sherry, A.D., 2015. Basic MR relaxation mechanisms and contrast agent design. J. Magn. Reson. Imaging 42, 545–565. https://doi.org/10.1002/jmri.24787.

Dehkordi, A.N.V., Kamali-Asl, A., Wen, N., Mikkelsen, T., Chetty, I.J., Bagher-Ebadian, H., 2017. DCE-MRI prediction of survival time for patients with glioblastoma

multiforme: using an adaptive neuro-fuzzy-based model and nested model selection technique. NMR Biomed. 30 https://doi.org/10.1002/nbm.3739.
Dennie, J., Mandeville, J.B., Boxerman, J.L., Packard, S.D., Rosen, B.R., Weisskoff, R.M., 1998. NMR imaging of changes in vascular morphology due to tumor angiogenesis. Magn. Reson. Med. 40, 793–799. https://doi.org/10.1002/mrm.1910400602.
Digernes, I., Bjørnerud, A., Vatnehol, S.A.S., Løvland, G., Courivaud, F., Vik-Mo, E., Meling, T.R., Emblem, K.E., 2017. A theoretical framework for determining cerebral vascular function and heterogeneity from dynamic susceptibility contrast MRI. J. Cereb. Blood Flow. Metab. 37, 2237–2248. https://doi.org/10.1177/0271678X17694187.
Donahue, K.M., Krouwer, H.G.J., Rand, S.D., Pathak, A.P., Marszalkowski, C.S., Censky, S.C., Prost, R.W., 2000. Utility of simultaneously acquired gradient-echo and spin-echo cerebral blood volume and morphology maps in brain tumor patients. Magn. Reson. Med. 43, 845–853. https://doi.org/10.1002/1522-2594(200006)43:6<845::Aid-Mrm10>3.0.Co;2-J.
Eichner, C., Jafari-Khouzani, K., Cauley, S., Bhat, H., Polaskova, P., Andronesi, O.C., Rapalino, O., Turner, R., Wald, L.L., Stufflebeam, S., Setsompop, K., 2014. Slice accelerated gradient-echo spin-echo dynamic susceptibility contrast imaging with blipped CAIPI for increased slice coverage. Magn. Reson. Med. 72, 770–778. https://doi.org/10.1002/mrm.24960.
Emblem, K.E., Mouridsen, K., Bjornerud, A., Farrar, C.T., Jennings, D., Borra, R.J., Wen, P.Y., Ivy, P., Batchelor, T.T., Rosen, B.R., Jain, R.K., Sorensen, A.G., 2013. Vessel architectural imaging identifies cancer patient responders to anti-angiogenic therapy. Nat. Med. 19, 1178–1183. https://doi.org/10.1038/nm.3289.
Engvall, C., Ryding, E., Wirestam, R., Holtås, S., Ljunggren, K., Ohlsson, T., Reinstrup, P., 2008. Human cerebral blood volume (CBV) measured by dynamic susceptibility contrast MRI and 99mTc-RBC SPECT. J. Neurosurg. Anesthesiol. 20, 41–44.
Eskildsen, S.F., Gyldensted, L., Nagenthiraja, K., Nielsen, R.B., Hansen, M.B., Dalby, R.B., Frandsen, J., Rodell, A., Gyldensted, C., Jespersen, S.N., Lund, T.E., Mouridsen, K., Braendgaard, H., Ostergaard, L., 2017. Increased cortical capillary transit time heterogeneity in Alzheimer's disease: a DSC-MRI perfusion study. Neurobiol. Aging 50, 107–118. https://doi.org/10.1016/j.neurobiolaging.2016.11.004.
Evelhoch, J.L., 1999. Key factors in the acquisition of contrast kinetic data for oncology. J. Magn. Reson. Imaging 10, 254–259. https://doi.org/10.1002/(SICI)1522-2586(199909)10:3<254::AID-JMRI5>3.0.CO;2–9.
Ewing, J.R., Bagher-Ebadian, H., 2013. Model selection in measures of vascular parameters using dynamic contrast-enhanced MRI: experimental and clinical applications. Nmr Biomed. 26, 1028–1041. https://doi.org/10.1002/nbm.2996.
Ewing, J.R., Knight, R.A., Nagaraja, T.N., Yee, J.S., Nagesh, V., Whitton, P.A., Li, L., Fenstermacher, J.D., 2003. Patlak plots of Gd-DTPA MRI data yield blood-brain transfer constants concordant with those of 14C-sucrose in areas of blood-brain opening. Magn. Reson. Med. 50, 283–292. https://doi.org/10.1002/mrm.10524.
Farrall, A.J., Wardlaw, J.M., 2009. Blood-brain barrier: ageing and microvascular disease–systematic review and meta-analysis. Neurobiol. Aging 30, 337–352. https://doi.org/10.1016/j.neurobiolaging.2007.07.015.
Ferreira, R.M., Lev, M.H., Goldmakher, G.V., Kamalian, S., Schaefer, P.W., Furie, K.L., Gonzalez, R.G., Sanelli, P.C., 2010. Arterial input function placement for accurate CT perfusion map construction in acute stroke. AJR Am. J. Roentgenol. 194, 1330–1336.
Fluckiger, J.U., Schabel, M.C., DiBella, E.V.R., 2010. Toward local arterial input functions in dynamic contrast-enhanced MRI. J. Magn. Reson. Imaging 32, 924–934. https://doi.org/10.1002/jmri.22339.
Francis, P.L., Jakubovic, R., O'Connor, P., Zhang, L., Eilaghi, A., Lee, L., Carroll, T.J., Mouannes-Srour, J., Feinstein, A., Aviv, R.I., 2013. Robust perfusion deficits in cognitively impaired patients with secondary-progressive multiple sclerosis. AJNR Am. J. Neuroradiol. 34, 62–67. https://doi.org/10.3174/ajnr.A3148.
Frenzel, T., Lengsfeld, P., Schirmer, H., Hütter, J., Weinmann, H.-J., 2008. Stability of gadolinium-based magnetic resonance imaging contrast agents in human serum at 37°C. Invest.. Radiol. 43, 817–828. https://doi.org/10.1097/RLI.0b013e3181852171.
Frøhlich, A.F., Østergaard, L., Kiselev, V.G., 2005. Theory of susceptibility-induced transverse relaxation in the capillary network in the diffusion narrowing regime. Magn. Reson. Med. 53, 564–573. https://doi.org/10.1002/mrm.20394.
Fuss, M., Wenz, F., Essig, M., Muenter, M., Debus, J., Herman, T.S., Wannenmacher, M., 2001. Tumor angiogenesis of low-grade astrocytomas measured by dynamic susceptibility contrast-enhanced MRI (DSC-MRI) is predictive of local tumor control after radiation therapy. Int. J. Radiat. Oncol. Biol. Phys. 51, 478–482. https://doi.org/10.1016/S0360-3016(01)01691-1.
Gahramanov, S., Muldoon, L.L., Varallyay, C.G., Li, X., Kraemer, D.F., Fu, R., Hamilton, B.E., Rooney, W.D., Neuwelt, E.A., 2013. Pseudoprogression of glioblastoma after chemo- and radiation therapy: diagnosis by using dynamic susceptibility-weighted contrast-enhanced perfusion MR imaging with ferumoxytol versus gadoteridol and correlation with survival. Radiology 266, 842–852. https://doi.org/10.1148/radiol.12111472.
Gaitan, M.I., Shea, C.D., Evangelou, I.E., Stone, R.D., Fenton, K.M., Bielekova, B., Massacesi, L., Reich, D.S., 2011. Evolution of the blood-brain barrier in newly forming multiple sclerosis lesions. Ann. Neurol. 70, 22–29. https://doi.org/10.1002/ana.22472.
Ge, Y., Law, M., Johnson, G., Herbert, J., Babb, J.S., Mannon, L.J., Grossman, R.I., 2005. Dynamic susceptibility contrast perfusion MR imaging of multiple sclerosis lesions: characterizing hemodynamic impairment and inflammatory activity. Am. J. Neuroradiol. 26, 1539–1547.
Gelderen, P., van Grandin, C., Petrella, J.R., Moonen, C.T.W., 2000. Rapid three-dimensional MR imaging method for tracking a bolus of contrast agent through the brain. Radiology 216, 603–608. https://doi.org/10.1148/radiology.216.2.r00au27603.
Gharagouzloo, C.A., McMahon, P.N., Sridhar, S., 2015. Quantitative contrast-enhanced MRI with superparamagnetic nanoparticles using ultrashort time-to-echo pulse sequences. Magn. Reson. Med. 74, 431–441. https://doi.org/10.1002/mrm.25426.
Guo, Y., Lebel, R.M., Zhu, Y., Lingala, S.G., Shiroishi, M.S., Law, M., Nayak, K., 2016. High-resolution whole-brain DCE-MRI using constrained reconstruction: prospective clinical evaluation in brain tumor patients. Med. Phys. 43, 2013. https://doi.org/10.1118/1.4944736.
Haacke, E.M., Filleti, C.L., Gattu, R., Ciulla, C., Al-Bashir, A., Suryanarayanan, K., Li, M., Latif, Z., DelProposto, Z., Sehgal, V., Li, T., Torquato, V., Kanaparti, R., Jiang, J., Neelavalli, J., 2007. New algorithm for quantifying vascular changes in dynamic contrast-enhanced MRI independent of absolute T1 values. Magn. Reson. Med. 58, 463–472. https://doi.org/10.1002/mrm.21358.
Haar, H.J., van de Burgmans, S., Jansen, J.F.A., Osch, M.J.P., van Buchem, M.A., van Muller, M., Hofman, P.A.M., Verhey, F.R.J., Backes, W.H., 2016. Blood-brain barrier leakage in patients with early alzheimer disease. Radiology 281, 527–535. https://doi.org/10.1148/radiol.2016152244.
Hakyemez, B., Erdogan, C., Ercan, I., Ergin, N., Uysal, S., Atahan, S., 2005. High-grade and low-grade gliomas: differentiation by using perfusion MR imaging. Clin. Radiol. 60, 493–502. https://doi.org/10.1016/j.crad.2004.09.009.
Heye, A.K., Culling, R.D., Valdes Hernandez Mdel, C., Thrippleton, M.J., Wardlaw, J.M., 2014. Assessment of blood-brain barrier disruption using dynamic contrast-enhanced MRI. A systematic review. Neuroimage Clin. 6, 262–274. https://doi.org/10.1016/j.nicl.2014.09.002.
Hu, L.S., Baxter, L.C., Pinnaduwage, D.S., Paine, T.L., Karis, J.P., Feuerstein, B.G., Schmainda, K.M., Dueck, A.C., Debbins, J., Smith, K.A., Nakaji, P., Eschbacher, J.M., Coons, S.W., Heiserman, J.E., 2010. Optimized preload leakage-correction methods to improve the diagnostic accuracy of dynamic susceptibility-weighted contrast-enhanced perfusion MR imaging in posttreatment gliomas. Am. J. Neuroradiol. 31, 40–48.
Hu, L.S., Kelm, Z., Korfiatis, P., Dueck, A.C., Elrod, C., Ellingson, B.M., Kaufmann, T.J., Eschbacher, J.M., Karis, J.P., Smith, K., Nakaji, P., Brinkman, D., Pafundi, D., Baxter, L.C., Erickson, B.J., 2015. Impact of software modeling on the accuracy of perfusion MRI in glioma. AJNR Am. J. Neuroradiol. 36, 2242–2249. https://doi.org/10.3174/ajnr.A4451.
Huang, W., Chen, Y., Fedorov, A., Li, X., Jajamovich, G.H., Malyarenko, D.I., Aryal, M.P., LaViolette, P.S., Oborski, M.J., O'Sullivan, F., Abramson, R.G., Jafari-Khouzani, K., Afzal, A., Tudorica, A., Moloney, B., Gupta, S.N., Besa, C., Kalpathy-Cramer, J., Mountz, J.M., Laymon, C.M., Muzi, M., Schmainda, K., Cao, Y., Chenevert, T.L., Taouli, B., Yankeelov, T.E., Fennessy, F., Li, X., 2016. The impact of arterial input function determination variations on prostate dynamic contrast-enhanced magnetic resonance imaging pharmacokinetic modeling: a multicenter data analysis challenge. Tomogr. a J. imaging Res. 2, 56–66. https://doi.org/10.18383/j.tom.2015.00184.
Ielacqua, G.D., Schlegel, F., Fuchtemeier, M., Xandry, J., Rudin, M., Klohs, J., 2015. Magnetic resonance Q mapping reveals a decrease in microvessel density in the arcAbeta mouse model of cerebral amyloidosis. Front. Aging Neurosci. 7, 241. https://doi.org/10.3389/fnagi.2015.00241.
Inglese, M., Adhya, S., Johnson, G., Babb, J.S., Miles, L., Jaggi, H., Herbert, J., Grossman, R.I., 2008. Perfusion magnetic resonance imaging correlates of neuropsychological impairment in multiple sclerosis. J. Cereb. Blood Flow. Metab. 28, 164–171. https://doi.org/10.1038/sj.jcbfm.9600504.
Inglese, M., Park, S., Johnson, G., et al., 2007. Deep gray matter perfusion in multiple sclerosis: dynamic susceptibility contrast perfusion magnetic resonance imaging at 3 t. Arch. Neurol. 64, 196–202. https://doi.org/10.1001/archneur.64.2.196.
Ingrisch, M., Sourbron, S., Morhard, D., Ertl-Wagner, B., Kümpfel, T., Hohlfeld, R., Reiser, M., Glaser, C., 2012. Quantification of perfusion and permeability in multiple sclerosis: dynamic contrast-enhanced MRI in 3D at 3T. Invest. Radiol. 47, 252–258. https://doi.org/10.1097/RLI.0b013e31823bfc97.
Jelescu, I.O., Leppert, I.R., Narayanan, S., Araujo, D., Arnold, D.L., Pike, G.B., 2011. Dual-temporal resolution dynamic contrast-enhanced MRI protocol for blood-brain barrier permeability measurement in enhancing multiple sclerosis lesions. J. Magn. Reson Imaging 33, 1291–1300. https://doi.org/10.1002/jmri.22565.
Jensen, J.H., Chandra, R., 2000. MR imaging of microvasculature. Magn. Reson. Med. 44, 224–230. https://doi.org/10.1002/1522-2594(200008)44:2<224::AID-MRM9>3.0.CO;2-M.
Jespersen, S.N., Ostergaard, L., 2012. The roles of cerebral blood flow, capillary transit time heterogeneity, and oxygen tension in brain oxygenation and metabolism. J. Cereb. Blood Flow. Metab. 32, 264–277. https://doi.org/10.1038/jcbfm.2011.153.
Jochimsen, T.H., Newbould, R.D., Skare, S.T., Clayton, D.B., Albers, G.W., Moseley, M.E., Bammer, R., 2007. Identifying systematic errors in quantitative dynamic-susceptibility contrast perfusion imaging by high-resolution multi-echo parallel EPI. Nmr Biomed. 20, 429–438. https://doi.org/10.1002/nbm.1107.
Johnson, G., Wetzel, S.G., Cha, S., Babb, J., Tofts, P.S., 2004. Measuring blood volume and vascular transfer constant from dynamic, T(2)*-weighted contrast-enhanced MRI. Magn. Reson. Med. 51, 961–968. https://doi.org/10.1002/mrm.20049.
Johnson, N.A., Jahng, G.-H., Weiner, M.W., Miller, B.L., Chui, H.C., Jagust, W.J., Gorno-Tempini, M.L., Schuff, N., 2005. Pattern of cerebral hypoperfusion in alzheimer disease and mild cognitive impairment measured with arterial spin-labeling MR imaging: initial experience. Radiology 234, 851–859. https://doi.org/10.1148/radiol.2343040197.
Jonathan, S.V., Vakil, P., Jeong, Y., Ansari, S., Hurley, M., Bendok, B., Carroll, T.J., 2013. A radial 3D GRE-EPI pulse sequence with kz blip encoding for whole-brain isotropic 3D perfusion using DSC-MRI bolus tracking with sliding window reconstruction (3D RAZIR). In: Proceedings of the 21st Annual Meeting of ISMRM. Salt Lake City, UT, USA, p. 582.
Kanda, T., Fukusato, T., Matsuda, M., Toyoda, K., Oba, H., Kotoku, J., Haruyama, T., Kitajima, K., Furui, S., 2015. Gadolinium-based contrast agent accumulates in the

brain even in subjects without severe renal dysfunction: evaluation of autopsy brain specimens with inductively coupled plasma mass spectroscopy. Radiology 276, 228–232. https://doi.org/10.1148/radiol.2015142690.
Kety, S.S., 1951. The theory and applications of the exchange of inert gas at the lungs and tissues. Pharmacol. Rev. 3, 1–41.
Kim, E., Cebulla, J., Ward, B.D., Rhie, K., Zhang, J., Pathak, A.P., 2013. Assessing breast cancer angiogenesis in vivo: which susceptibility contrast MRI biomarkers are relevant? Magn. Reson. Med. 70, 1106–1116. https://doi.org/10.1002/mrm.24530.
Kiselev, V.G., 2001. On the theoretical basis of perfusion measurements by dynamic susceptibility contrast MRI. Magn. Reson. Med. 46, 1113–1122. https://doi.org/10.1002/mrm.1307.
Kjolby, B.F., Ostergaard, L., Kiselev, V.G., 2006. Theoretical model of intravascular paramagnetic tracers effect on tissue relaxation. Magn. Reson. Med. 56, 187–197. https://doi.org/10.1002/mrm.20920.
Knutsson, L., Stahlberg, F., Wirestam, R., 2004. Aspects on the accuracy of cerebral perfusion parameters obtained by dynamic susceptibility contrast MRI: a simulation study. Magn. Reson. Imaging 22, 789–798. https://doi.org/10.1016/j.mri.2003.12.002.
Kosior, J.C., Frayne, R., 2010. Perfusion parameters derived from bolus-tracking perfusion imaging are immune to tracer recirculation. J. Magn. Reson Imaging 31, 753–756. https://doi.org/10.1002/jmri.22052.
Kuperman, V.Y.U., Karczmar, G.S., Blomley, M.J.K., Lewis, M.Z., Lubich, L.M., Lipton, M.J., 1996. Differentiating between T1 and T2* changes caused by gadopentetate dimeglumine in the kidney by using a double-echo dynamic MR imaging sequence. J. Magn. Reson. Imaging 6, 764–768. https://doi.org/10.1002/jmri.1880060509.
Kuschinsky, W., Paulson, O.B., 1992. Capillary circulation in the brain. Cerebrovasc. Brain Metab. Rev. 4, 261–286.
Landis, C.S., Li, X., Telang, F.W., Coderre, J.A., Micca, P.L., Rooney, W.D., Latour, L.L., Vetek, G., Palyka, I., Springer, C.S., 2000. Determination of the MRI contrast agent concentration time course in vivo following bolus injection: effect of equilibrium transcytolemmal water exchange. Magn. Reson. Med. 44, 563–574. https://doi.org/10.1002/1522-2594(200010)44:4<563::Aid-Mrm10>3.0.Co;2-#.
Lansberg, M.G., Lee, J., Christensen, S., Straka, M., De Silva, D.A., Mlynash, M., Campbell, B.C., Bammer, R., Olivot, J.M., Desmond, P., Davis, S.M., Donnan, G.A., Albers, G.W., 2011. RAPID automated patient selection for reperfusion therapy: a pooled analysis of the echoplanar imaging thrombolytic evaluation trial (EPITHET) and the diffusion and perfusion imaging evaluation for understanding stroke evolution (DEFUSE) study. Stroke 42, 1608–1614. https://doi.org/10.1161/STROKEAHA.110.609008.
Larsson, C., Kleppesto, M., Rasmussen Jr., I., Salo, R., Vardal, J., Brandal, P., Bjornerud, A., 2013. Sampling requirements in DCE-MRI based analysis of high grade gliomas: simulations and clinical results. J. Magn. Reson Imaging 37, 818–829. https://doi.org/10.1002/jmri.23866.
Larsson, H.B.W., Stubgaard, M., Frederiksen, J.L., Jensen, M., Henriksen, O., Paulson, O.B., 1990. Quantitation of blood-brain barrier defect by magnetic resonance imaging and gadolinium-DTPA in patients with multiple sclerosis and brain tumors. Magn. Reson. Med. 16, 117–131. https://doi.org/10.1002/mrm.1910160111.
Lauffer, R.B., 1987. Paramagnetic metal complexes as water proton relaxation agents for NMR imaging: theory and design. Chem. Rev. Wash. D.C. United States) 87, 901–927.
Lee, J.-H., Springer, C.S., 2003. Effects of equilibrium exchange on diffusion-weighted NMR signals: the diffusigraphic “shutter-speed”. Magn. Reson. Med. 49, 450–458.
Leenders, K.L., Perani, D., Lammertsma, A.A., Heather, J.D., Buckingham, P., Healy, M.J., Gibbs, J.M., Wise, R.J., Hatazawa, J., Herold, S., 1990. Cerebral blood flow, blood volume and oxygen utilization. Normal values and effect of age. Brain 113 (1), 27–47. https://doi.org/10.1093/brain/113.1.27.
Leiner, T., Kucharczyk, W., 2009. NSF prevention in clinical practice: summary of recommendations and guidelines in the United States, Canada, and Europe. J. Magn. Reson. Imaging 30, 1357–1363. https://doi.org/10.1002/jmri.22021.
Lemasson, B., Pannetier, N., Coquery, N., Boisserand, L.S.B., Collomb, N., Schuff, N., Moseley, M., Zaharchuk, G., Barbier, E.L., Christen, T., 2016. MR vascular fingerprinting in stroke and brain tumors models. Sci. Rep. 6 https://doi.org/10.1038/srep37071.
Lemasson, B., Valable, S., Farion, R., Krainik, A., Remy, C., Barbier, E.L., 2013. In vivo imaging of vessel diameter, size, and density: a comparative study between MRI and histology. Magn. Reson. Med. 69, 18–26. https://doi.org/10.1002/mrm.24218.
Leu, K., Boxerman, J.L., Cloughesy, T.F., Lai, A., Nghiemphu, P.L., Liau, L.M., Pope, W.B., ellingson, B.M., 2016. Improved leakage correction for single-echo dynamic susceptibility contrast perfusion MRI estimates of relative cerebral blood volume in high-grade gliomas by accounting for bidirectional contrast agent exchange. Am. J. Neuroradiol. 37, 1440–1446.
Li, X., Zhu, Y., Kang, H., Zhang, Y., Liang, H., Wang, S., Zhang, W., 2015. Glioma grading by microvascular permeability parameters derived from dynamic contrast-enhanced MRI and intratumoral susceptibility signal on susceptibility weighted imaging. Cancer Imaging 15, 4.
Liu, H.-L., Pu, Y., Liu, Y., Nickerson, L., Andrews, T., Fox, P.T., Gao, J.-H., 1999. Cerebral blood flow measurement by dynamic contrast MRI using singular value decomposition with an adaptive threshold. Magn. Reson. Med. 42, 167–172. https://doi.org/10.1002/(SICI)1522-2594(199907)42:1<167::AID-MRM22>3.0.CO;2-Q.
Maas, L.C., Harris, G.J., Satlin, A., English, C.D., Lewis, R.F., Renshaw, P.F., 1997. Regional Cereb. blood volume Meas. by Dyn. susceptibility contrast MR imaging alzheimer's. Dis. A Princ. components analysis 7, 219.
Mangla, R., Kolar, B., Zhu, T., Zhong, J., Almast, J., Ekholm, S., 2011. Percentage signal recovery derived from MR dynamic susceptibility contrast imaging is useful to differentiate common enhancing malignant lesions of the brain. AJNR Am. J. Neuroradiol. 32, 1004–1010. https://doi.org/10.3174/ajnr.A2441.
Mattia, D., Babiloni, F., Romigi, A., Cincotti, F., Bianchi, L., Sperli, F., Placidi, F., Bozzao, A., Giacomini, P., Floris, R., Grazia Marciani, M., 2003. Quantitative EEG and dynamic susceptibility contrast MRI in Alzheimer's disease: a correlative study. Clin. Neurophysiol. 114, 1210–1216. https://doi.org/10.1016/s1388-2457(03)00085-3.
McDonald, R.J., McDonald, J.S., Kallmes, D.F., Jentoft, M.E., Murray, D.L., Thielen, K.R., Williamson, E.E., Eckel, L.J., 2015. Intracranial gadolinium deposition after contrast-enhanced MR imaging. Radiology 275, 772–782. https://doi.org/10.1148/radiol.15150025.
Meier, P., Zierler, K.L., 1954. On the theory of the indicator-dilution method for measurement of blood flow and volume. J. Appl. Physiol. 6, 731–744.
Merali, Z., Huang, K., Mikulis, D., Silver, F., Kassner, A., 2017. Evolution of blood-brain-barrier permeability after acute ischemic stroke. PLoS One 12. https://doi.org/10.1371/journal.pone.0171558.
Metry, G., Wikström, B., Valind, S., Sandhagen, B., Linde, T., Beshara, S., Långström, B., Danielson, B.G., 1999. Effect of normalization of hematocrit on brain circulation and metabolism in hemodialysis patients. J. Am. Soc. Nephrol. 10, 854–863.
Montagne, A., Barnes, S.R., Sweeney, M.D., Halliday, M.R., Sagare, A.P., Zhao, Z., Toga, A.W., Jacobs, R.E., Liu, C.Y., Amezcua, L., Harrington, M.G., Chui, H.C., Law, M., Zlokovic, B.V., 2015. Blood-brain barrier breakdown in the aging human hippocampus. Neuron 85, 296–302. https://doi.org/10.1016/j.neuron.2014.12.032.
Mouridsen, K., Friston, K., Hjort, N., Gyldensted, L., Østergaard, L., Kiebel, S., 2006. Bayesian estimation of cerebral perfusion using a physiological model of microvasculature. Neuroimage 33, 570–579. https://doi.org/10.1016/j.neuroimage.2006.06.015.
Mouridsen, K., Hansen, M.B., Ostergaard, L., Jespersen, S.N., 2014. Reliable estimation of capillary transit time distributions using DSC-MRI. J. Cereb. Blood Flow. Metab. 34, 1511–1521. https://doi.org/10.1038/jcbfm.2014.111.
Nasseri, M., Gahramanov, S., Netto, J.P., Fu, R., Muldoon, L.L., Varallyay, C., Hamilton, B.E., Neuwelt, E.A., 2014. Evaluation of pseudoprogression in patients with glioblastoma multiforme using dynamic magnetic resonance imaging with ferumoxytol calls RANO criteria into question. Neuro. Oncol.
Nejad-Davarani, S.P., Bagher-Ebadian, H., Ewing, J.R., Noll, D.C., Mikkelsen, T., Chopp, M., Jiang, Q., 2017a. An extended vascular model for less biased estimation of permeability parameters in DCE-T1 images. NMR Biomed 30. https://doi.org/10.1002/nbm.3698.
Nejad-Davarani, S.P., Bagher-Ebadian, H., Ewing, J.R., Noll, D.C., Mikkelsen, T., Chopp, M., Jiang, Q., 2017b. A parametric model of the brain vascular system for estimation of the arterial input function (AIF) at the tissue level. NMR Biomed 30. https://doi.org/10.1002/nbm.3695.
Newbould, R.D., Skare, S.T., Jochimsen, T.H., Alley, M.T., Moseley, M.E., Albers, G.W., Bammer, R., 2007. Perfusion mapping with multiecho multishot parallel imaging EPI. Magn. Reson. Med. 58, 70–81. https://doi.org/10.1002/mrm.21255.
Newton, A.T., Pruthi, S., Stokes, A.M., Skinner, J.T., Quarles, C.C., 2016. Improving perfusion measurement in DSC-MR imaging with multiecho information for arterial input function determination. In: American Journal of Neuroradiology, pp. 1237–1243. https://doi.org/10.3174/ajnr.A4700.
Nielsen, R.B., Egefjord, L., Angleys, H., Mouridsen, K., Gejl, M., Moller, A., Brock, B., Braendgaard, H., Gottrup, H., Rungby, J., Eskildsen, S.F., Ostergaard, L., 2017. Capillary dysfunction is associated with symptom severity and neurodegeneration in Alzheimer's disease. Alzheimers Dement. https://doi.org/10.1016/j.jalz.2017.02.007.
Oesterle, C., Strohschein, R., Köhler, M., Schnell, M., Hennig, J., 2000. Benefits and pitfalls of keyhole imaging, especially in first-pass perfusion studies. J. Magn. Reson. Imaging 11, 312–323. https://doi.org/10.1002/(SICI)1522-2586(200003)11:3<312::AID-JMRI10>3.0.CO;2-K.
Østergaard, L., Aamand, R., Gutiérrez-Jiménez, E., Ho, Y.-C.L., Blicher, J.U., Madsen, S.M., Nagenthiraja, K., Dalby, R.B., Drasbek, K.R., Møller, A., Brændgaard, H., Mouridsen, K., Jespersen, S.N., Jensen, M.S., West, M.J., 2013. The capillary dysfunction hypothesis of Alzheimer's disease. Neurobiol. Aging 34, 1018–1031. https://doi.org/10.1016/j.neurobiolaging.2012.09.011.
Østergaard, L., Johannsen, P., Høst-Poulsen, P., Vestergaard-Poulsen, P., Asboe, H., Gee, A.D., Hansen, S.B., Cold, G.E., Gjedde, A., Gyldensted, C., 1998a. Cerebral blood flow measurements by magnetic resonance imaging bolus tracking: comparison with [15O]H2O positron emission tomography in humans. J. Cereb. Blood Flow. Metab. 18, 935–940. https://doi.org/10.1097/00004647-199809000-00002.
Østergaard, L., Smith, D.F., Vestergaard-Poulsen, P., Hansen, S., Gee, A.D., Gjedde, A., Gyldensted, C., 1998b. Absolute cerebral blood flow and blood volume measured by magnetic resonance imaging bolus tracking: comparison with positron emission tomography values. J. Cereb. Blood Flow. Metab. 18, 425–432. https://doi.org/10.1097/00004647-199804000-00011.
Ostergaard, L., Sorensen, A., Kwong, K., Weisskoff, R., Gyldensted, C., Rosen, B., 1996a. High resolution measurement of cerebral blood flow using intravascular tracer bolus passages. Part II: experimental comparison and preliminary results. Magn. Reson. Med. 36, 726–736.
Ostergaard, L., Sorensen, A.G., Chesler, D.A., Weisskoff, R.M., Koroshetz, W.J., Wu, O., Gyldensted, C., Rosen, B.R., 2000. Combined diffusion-weighted and perfusion-weighted flow heterogeneity magnetic resonance imaging in acute stroke. Stroke 31, 1097–1103. https://doi.org/10.1161/01.STR.31.5.1097.
Ostergaard, L., Tietze, A., Nielsen, T., Drasbek, K.R., Mouridsen, K., Jespersen, S.N., Horsman, M.R., 2013. The relationship between tumor blood flow, angiogenesis, tumor hypoxia, and aerobic glycolysis. Cancer Res. https://doi.org/10.1158/0008-5472.CAN-13-0964.
Ostergaard, L., Weisskoff, R.M., Chesler, D.A., Gyldensted, C., Rosen, B.R., 1996b. High resolution measurement of cerebral blood flow using intravascular tracer bolus

passages. Part I: mathematical approach and statistical analysis. Magn. Reson. Med. 36, 715–725.
Pathak, A., Kim, Y.R., Donahue, K., 2002. The effect of brain tumor angiogenesis on the in vivo relationship between contrast agent (MION) dose and the gradient echo relaxation rate change. In: International Society of Magnetic Resonance in Medicine, p. 312.
Paulson, E.S., Prah, D.E., Schmainda, K.M., 2016. Spiral perfusion imaging with consecutive echoes (SPICE) for the simultaneous mapping of DSC- and DCE-MRI parameters in brain tumor patients: theory and initial feasibility. Tomography 2, 295–307. https://doi.org/10.18383/j.tom.2016.00217.
Paulson, E.S., Schmainda, K.M., 2008. Comparison of dynamic susceptibility-weighted contrast-enhanced MR methods: recommendations for measuring relative cerebral blood volume in brain tumors. Radiology 249, 601–613. https://doi.org/10.1148/radiol.2492071659.
Pedersen, M., Klarhofer, M., Christensen, S., Ouallet, J.C., Ostergaard, L., Dousset, V., Moonen, C., 2004. Quantitative cerebral perfusion using the PRESTO acquisition scheme. J. Magn. Reson Imaging 20, 930–940. https://doi.org/10.1002/jmri.20206.
Peruzzo, D., Castellaro, M., Calabrese, M., Veronese, E., Rinaldi, F., Bernardi, V., Favaretto, A., Gallo, P., Bertoldo, A., 2013. Heterogeneity of cortical lesions in multiple sclerosis: an MRI perfusion study. J. Cereb. Blood Flow. Metab. 33, 457–463. https://doi.org/10.1038/jcbfm.2012.192.
Prah, M.A., Stufflebeam, S.M., Paulson, E.S., Kalpathy-Cramer, J., Gerstner, E.R., Batchelor, T.T., Barboriak, D.P., Rosen, B.R., Schmainda, K.M., 2015. Repeatability of standardized and normalized relative CBV in patients with newly diagnosed glioblastoma. Am. J. Neuroradiol. 36, 1654–1661. https://doi.org/10.3174/ajnr.A4374.
QIBA, 2012. QIBA DCE-mri Biomarker Committee. DCE MRI Quantification Profile, Quantitative Imaging Biomarkers Alliance. Version 1.0 Profile Stage: Closed. QIBA August 2012.
Quarles, C.C., Gochberg, D.F., Gore, J.C., Yankeelov, T.E., 2009. A theoretical framework to model DSC-MRI data acquired in the presence of contrast agent extravasation. Phys. Med. Biol. 54, 5749–5766. https://doi.org/10.1088/0031-9155/54/19/006.
Quarles, C.C., Gore, J.C., Xu, L., Yankeelov, T.E., 2012. Comparison of dual-echo DSC-MRI- and DCE-MRI-derived contrast agent kinetic parameters. Magn. Reson. Imaging 30, 944–953. https://doi.org/10.1016/j.mri.2012.03.008.
Quarles, C.C., Schmainda, K.M., 2007. Assessment of the morphological and functional effects of the anti-angiogenic agent SU11657 on 9L gliosarcoma vasculature using dynamic susceptibility contrast MRI. Magn. Reson. Med. 57, 680–687. https://doi.org/10.1002/mrm.21193.
Quarles, C.C., Ward, B.D., Schmainda, K.M., 2005. Improving the reliability of obtaining tumor hemodynamic parameters in the presence of contrast agent extravasation. Magn. Reson. Med. 53, 1307–1316. https://doi.org/10.1002/mrm.20497.
Rempp, K.A., Brix, G., Wenz, F., Becker, C.R., Gückel, F., Lorenz, W.J., 1994. Quantification of regional cerebral blood flow and volume with dynamic susceptibility contrast-enhanced MR imaging. Radiology 193, 637–641. https://doi.org/10.1148/radiology.193.3.7972800.
Renshaw, P.F., Owen, C.S., McLaughlin, a C., Frey, T.G., Leigh, J.S., 1986. Ferromagnetic contrast agents: a new approach. Magn. Reson. Med. 3, 217–225. https://doi.org/10.1002/mrm.1910030205.
Rivera-Rivera, L.A., Schubert, T., Knobloch, G., Turski, P.A., Wieben, O., Reeder, S.B., Johnson, K.M., 2018. Comparison of ferumoxytol-based cerebral blood volume estimates using quantitative R1 and R2* relaxometry. Magn. Reson. Med. https://doi.org/10.1002/mrm.26975 (in press).
Rohrer, M., Bauer, H., Mintorovitch, J., Requardt, M., Weinmann, H.-J., 2005. Comparison of magnetic properties of MRI contrast media solutions at different magnetic field strengths. Invest. Radiol. 40, 715–724.
Rooney, W.D., Li, X., Sammi, M.K., Bourdette, D.N., Neuwelt, E.A., Springer, C.S., 2015. Mapping human brain capillary water lifetime: high-resolution metabolic neuroimaging. NMR Biomed. 28, 607–623. https://doi.org/10.1002/nbm.3294.
Rossi Espagnet, M.C., Bangiyev, L., Haber, M., Block, K.T., Babb, J., Ruggiero, V., Boada, F., Gonen, O., Fatterpekar, G.M., 2015. High-resolution DCE-MRI of the pituitary gland using radial k-space acquisition with compressed sensing reconstruction. AJNR Am. J. Neuroradiol. 36, 1444–1449. https://doi.org/10.3174/ajnr.A4324.
Ryu, W.H.A., Avery, M.B., Dharampal, N., Allen, I.E., Hetts, S.W., 2016. Utility of perfusion imaging in acute stroke treatment: a systematic review and meta-analysis. J. Neurointerv. Surg. neurintsurg. https://doi.org/10.1136/neurintsurg-2016-012751, 2016–012751.
Sandoval, K.E., Witt, K.A., 2008. Blood-brain barrier tight junction permeability and ischemic stroke. Neurobiol. Dis. https://doi.org/10.1016/j.nbd.2008.08.005.
Schabel, M.C., Fluckiger, J.U., DiBella, E.V.R., 2010. A model-constrained Monte Carlo method for blind arterial input function estimation in dynamic contrast-enhanced MRI: I. Simulations. Phys. Med. Biol 55, 4783–4806. https://doi.org/10.1088/0031-9155/55/16/011.
Schabel, M.C., Parker, D.L., 2008. Uncertainty and bias in contrast concentration measurements using spoiled gradient echo pulse sequences. Phys. Med. Biol. 53, 2345.
Schmainda, K., Prah, M., Rand, S., Liu, Y., Logan, B., Muzi, M., Rane, S., Da, X., Yen, Y., Kalpathy-Cramer, J., Chenevert, T., Hoff, B., Ross, B., Cao, Y., Aryal, M., Erickson, B., Korfiatis, P., Dondlinger, B., Bell, L., Hu, L., Quarles, C., 2018. Multi-site concordance of DSC-MRI analysis for brain tumors: results of a NCI quantitative imaging network collaborative project. Am. J. Neuroradiol. (in press).
Schmainda, K.M., Prah, M., Baxter, L.C., Paulson, E.S., Maze, S., Pipe, J., Wang, D., Debbins, J., Hu, L.S., 2015a. Simultaneous measurement of DSC- and DCE-MRI parameters using dual-echo spiral with a standard dose of gadolinium in comparison to single-echo GRE-EPI methods in brain tumors. In: Proceedings of the 23rd Annual Meeting of ISMRM. Toronto, Ontario, Canada, p. 487.
Schmainda, K.M., Rand, S.D., Joseph, A.M., Lund, R., Ward, B.D., Pathak, A.P., Ulmer, J.L., Baddrudoja, M.A., Krouwer, H.G.J., 2004. Characterization of a first-pass gradient-echo spin-echo method to predict brain tumor grade and angiogenesis. Am. J. Neuroradiol. 25, 1524–1532.
Schmainda, K.M., Zhang, Z., Prah, M., Snyder, B.S., Gilbert, M.R., Sorensen, A.G., Barboriak, D.P., Boxerman, J.L., 2015b. Dynamic susceptibility contrast MRI measures of relative cerebral blood volume as a prognostic marker for overall survival in recurrent glioblastoma: results from the ACRIN 6677/RTOG 0625 multicenter trial. Neuro Oncol. 17, 1148–1156. https://doi.org/10.1093/neuonc/nou364.
Schmiedeskamp, H., Andre, J.B., Straka, M., Christen, T., Nagpal, S., Recht, L., Thomas, R.P., Zaharchuk, G., Bammer, R., 2013. Simultaneous perfusion and permeability measurements using combined spin- and gradient-echo MRI. J. Cereb. Blood Flow. Metab. 33, 732–743. https://doi.org/10.1038/jcbfm.2013.10.
Schmiedeskamp, H., Straka, M., Newbould, R.D., Zaharchuk, G., Andre, J.B., Olivot, J.M., Moseley, M.E., Albers, G.W., Bammer, R., 2012. Combined spin- and gradient-echo perfusion-weighted imaging. Magn. Reson. Med. 68, 30–40. https://doi.org/10.1002/mrm.23195.
Semmineh, N.B., Stokes, A.M., Bell, L.C., Boxerman, J.L., Quarles, C.C., 2017. A population-based digital reference object (DRO) for optimizing dynamic susceptibility contrast (DSC)-MRI methods for clinical trials. Tomography 3, 41–49. https://doi.org/10.18383/j.tom.2016.00286.
Semmineh, N.B., Xu, J., Boxerman, J.L., Delaney, G.W., Cleary, P.W., Gore, J.C., Quarles, C.C., 2014. An efficient computational approach to characterize DSC-MRI signals arising from three-dimensional heterogeneous tissue structures. PLoS One 9, e84764. https://doi.org/10.1371/journal.pone.0084764.
Semmineh, N.B., Xu, J., Skinner, J.T., Xie, J., Li, H., Ayers, G., Quarles, C.C., 2015. Assessing tumor cytoarchitecture using multiecho DSC-MRI derived measures of the transverse relaxivity at tracer equilibrium (TRATE). Magn. Reson. Med. 74, 772–784. https://doi.org/10.1002/mrm.25435.
Shi, L., Wang, D., Liu, W., Fang, K., Wang, Y.-X.J., Huang, W., King, A.D., Heng, P.A., Ahuja, A.T., 2014. Automatic detection of arterial input function in dynamic contrast enhanced MRI based on affinity propagation clustering. J. Magn. Reson. Imaging 39, 1327–1337. https://doi.org/10.1002/jmri.24259.
Shinohara, R.T., Crainiceanu, C.M., Caffo, B.S., Gaitan, M.I., Reich, D.S., 2011. Population-wide principal component-based quantification of blood-brain-barrier dynamics in multiple sclerosis. Neuroimage 57, 1430–1446. https://doi.org/10.1016/j.neuroimage.2011.05.038.
Skinner, J.T., Robison, R.K., Elder, C.P., Newton, A.T., Damon, B.M., Quarles, C.C., 2014. Evaluation of a multiple spin- and gradient-echo (SAGE) EPI acquisition with SENSE acceleration: applications for perfusion imaging in and outside the brain. Magn. Reson. Imaging 32, 1171–1180. https://doi.org/10.1016/j.mri.2014.08.032.
Smith, D.S., Li, X., Gambrell, J.V., Arlinghaus, L.R., Quarles, C.C., Yankeelov, T.E., Welch, E.B., 2012. Robustness of quantitative compressive sensing MRI: the effect of random undersampling patterns on derived parameters for DCE- and DSC-MRI. IEEE Trans. Med. Imaging 31, 504–511. https://doi.org/10.1109/TMI.2011.2172216.
Sobesky, J., Zaro Weber, O., Lehnhardt, F.G., Hesselmann, V., Thiel, A., Dohmen, C., Jacobs, A., Neveling, M., Heiss, W.D., 2004. Which time-to-peak threshold best identifies penumbral flow? A comparison of perfusion-weighted magnetic resonance imaging and positron emission tomography in acute ischemic stroke. Stroke 35, 2843–2847. https://doi.org/10.1161/01.STR.0000147043.29399.f6.
Sourbron, S., Dujardin, M., Makkat, S., Luypaert, R., 2007a. Pixel-by-pixel deconvolution of bolus-tracking data: optimization and implementation. Phys. Med. Biol. 52, 429–447. https://doi.org/10.1088/0031-9155/52/2/009.
Sourbron, S., Heilmann, M., Biffar, A., Walczak, C., Vautier, J., Volk, A., Peller, M., 2009. Bolus-tracking MRI with a simultaneous T1- and T2*-measurement. Magn. Reson. Med. 62, 672–681. https://doi.org/10.1002/mrm.22042.
Sourbron, S., Luypaert, R., Morhard, D., Seelos, K., Reiser, M., Peller, M., 2007b. Deconvolution of bolus-tracking data: a comparison of discretization methods. Phys. Med. Biol. 52, 6761–6778. https://doi.org/10.1088/0031-9155/52/22/014.
Sourbron, S.P., Buckley, D.L., 2012. Tracer kinetic modelling in MRI: estimating perfusion and capillary permeability. Phys. Med. Biol. 57, R1–R33. https://doi.org/10.1088/0031-9155/57/2/R1.
Sowa, P., Bjornerud, A., Nygaard, G.O., Damangir, S., Spulber, G., Celius, E.G., Due-Tonnessen, P., Harbo, H.F., Beyer, M.K., 2015. Reduced perfusion in white matter lesions in multiple sclerosis. Eur. J. Radiol. 84, 2605–2612. https://doi.org/10.1016/j.ejrad.2015.09.007.
Springer, C.S., Broberg, C.S., Rooney, W.D., 2014. Taui, A high-resolution metabolic imaging biomarker for myocardium. J. Cardiovasc. Magn. Reson 16. https://doi.org/10.1186/1532-429X-16-S1-O111. O111.
Stables, L.A., Kennan, R.P., Gore, J.C., 1998. Asymmetric spin-echo imaging of magnetically inhomogeneous systems: theory, experiment, and numerical studies. Magn. Reson. Med. 40, 432–442.
Stanisz, G.J., Henkelman, R.M., 2000. Gd-DTPA relaxivity depends on macromolecular content. Magn. Reson. Med. 44, 665–667. https://doi.org/10.1002/1522-2594(200011)44:5<665::AID-MRM1>3.0.CO;2-M.
Starr, J.M., Farrall, A.J., Armitage, P., McGurn, B., Wardlaw, J., 2009. Blood-brain barrier permeability in Alzheimer's disease: a case-control MRI study. Psychiatry Res. 171, 232–241. https://doi.org/10.1016/j.pscychresns.2008.04.003.
Stikov, N., Boudreau, M., Levesque, I.R., Tardif, C.L., Barral, J.K., Pike, G.B., 2015. On the accuracy of T1 mapping: searching for common ground. Magn. Reson. Med. 73, 514–522. https://doi.org/10.1002/mrm.25135.

Stokes, A.M., Quarles, C.C., 2016. A simplified spin and gradient echo approach for brain tumor perfusion imaging. Magn. Reson. Med 75, 356–362. https://doi.org/10.1002/mrm.25591.

Stokes, A.M., Semmineh, N., Quarles, C.C., 2016a. Validation of a T1 and T2* leakage correction method based on multiecho dynamic susceptibility contrast MRI using MION as a reference standard. Magn. Reson. Med. 76, 613–625. https://doi.org/10.1002/mrm.25906.

Stokes, A.M., Skinner, J.T., Quarles, C.C., 2014. Assessment of a combined spin- and gradient-echo (SAGE) DSC-MRI method for preclinical neuroimaging. Magn. Reson. Imaging 32, 1181–1190. https://doi.org/10.1016/j.mri.2014.08.027.

Stokes, A.M., Skinner, J.T., Yankeelov, T.E., Quarles, C.C., 2016b. Assessment of a simplified spin and gradient echo (sSAGE) approach for human brain tumor perfusion imaging. Magn. Reson. Imaging 34, 1248–1255. https://doi.org/10.1016/j.mri.2016.07.004.

Taheri, S., Gasparovic, C., Shah, N.J., Rosenberg, G.A., 2011. Quantitative measurement of blood-brain barrier permeability in human using dynamic contrast-enhanced MRI with fast T1 mapping. Magn. Reson. Med. 65, 1036–1042. https://doi.org/10.1002/mrm.22686.

Thilmann, O., Larsson, E.M., Bjorkman-Burtscher, I.M., Stahlberg, F., Wirestam, R., 2004. Effects of echo time variation on perfusion assessment using dynamic susceptibility contrast MR imaging at 3 tesla. Magn. Reson. Imaging 22, 929–935. https://doi.org/10.1016/j.mri.2004.01.079.

Thompson, E.M., Guillaume, D.J., Dósa, E., Li, X., Nazemi, K.J., Gahramanov, S., Hamilton, B.E., Neuwelt, E.A., 2012. Dual contrast perfusion MRI in a single imaging session for assessment of pediatric brain tumors. J. Neurooncol.

Tietze, A., Mouridsen, K., Lassen-Ramshad, Y., Østergaard, L., 2015a. Perfusion MRI derived indices of microvascular shunting and flow control correlate with tumor grade and outcome in patients with cerebral glioma. PLoS One 10. https://doi.org/10.1371/journal.pone.0123044.

Tietze, A., Mouridsen, K., Mikkelsen, I.K., 2015b. The impact of reliable prebolus T 1 measurements or a fixed T 1 value in the assessment of glioma patients with dynamic contrast enhancing MRI. Neuroradiology 57, 561–572. https://doi.org/10.1007/s00234-015-1502-z.

Tofts, P.S., Brix, G., Buckley, D.L., Evelhoch, J.L., Henderson, E., Knopp, M.V., Larsson, H.B.W., Lee, T.-Y., Mayr, N.A., Parker, G.J.M., Port, R.E., Taylor, J., Weisskoff, R.M., 1999. Estimating kinetic parameters from dynamic contrast-enhanced t1-weighted MRI of a diffusable tracer: standardized quantities and symbols. J. Magn. Reson. Imaging 10, 223–232. https://doi.org/10.1002/(SICI)1522-2586(199909)10:3<223::AID-JMRI2>3.0.CO;2-S.

Tong, S., Hou, S., Zheng, Z., Zhou, J., Bao, G., 2010. Coating optimization of superparamagnetic iron oxide nanoparticles for high T2 relaxivity. Nano Lett. 10, 4607–4613. https://doi.org/10.1021/nl102623x.

Tóth, É., Helm, L., Merbach, A.E., 2002. Relaxivity of MRI contrast agents. Top. Curr. Chem. 221, 61–101. https://doi.org/10.1007/3-540-45733-X.

Toth, G.B., Varallyay, C.G., Horvath, A., Bashir, M.R., Choyke, P.L., Daldrup-Link, H.E., Dosa, E., Finn, J.P., Gahramanov, S., Harisinghani, M., Macdougall, I., Neuwelt, A., Vasanawala, S.S., Ambady, P., Barajas, R., Cetas, J.S., Ciporen, J., DeLoughery, T.J., Doolittle, N.D., Fu, R., Grinstead, J., Guimaraes, A.R., Hamilton, B.E., Li, X., McConnell, H.L., Muldoon, L.L., Nesbit, G., Netto, J.P., Petterson, D., Rooney, W.D., Schwartz, D., Szidonya, L., Neuwelt, E.A., 2017. Current and potential imaging applications of ferumoxytol for magnetic resonance imaging. Kidney Int. 92, 47–66. https://doi.org/10.1016/j.kint.2016.12.037.

Trapp, B.D., Nave, K.-A., 2008. Multiple sclerosis: an immune or neurodegenerative disorder? Annu. Rev. Neurosci. 31, 247–269. https://doi.org/10.1146/annurev.neuro.30.051606.094313.

Tropes, I., Grimault, S., Vaeth, A., Grillon, E., Julien, C., Payen, J.-F., Lamalle, L., Decorps, M., 2001. Vessel size imaging. Magn. Reson. Med. 45, 397–408.

Troprès, I., Grimault, S., Vaeth, A., Grillon, E., Julien, C., Payen, J.-F., Lamalle, L., Décorps, M., 2001. Vessel size imaging. Magn. Reson. Med. 45, 397–408. https://doi.org/10.1002/1522-2594(200103)45:3<397::AID-MRM1052>3.0.CO;2–3.

Tropres, I., Lamalle, L., Peoc'h, M., Farion, R., Usson, Y., Decorps, M., Remy, C., 2004. In vivo assessment of tumoral angiogenesis. Magn. Reson. Med. 51, 533–541. https://doi.org/10.1002/mrm.20017.

Troprès, I., Pannetier, N., Grand, S., Lemasson, B., Moisan, A., Péoc'h, M., Rémy, C., Barbier, E.L., 2015. Imaging the microvessel caliber and density: principles and applications of microvascular MRI. Magn. Reson. Med. 73, 325–341. https://doi.org/10.1002/mrm.25396.

van Osch, M.J., Vonken, E.J., Wu, O., Viergever, M.A., van der Grond, J., Bakker, C.J., 2003. Model of the human vasculature for studying the influence of contrast injection speed on cerebral perfusion MRI. Magn. Reson. Med. 50, 614–622. https://doi.org/10.1002/mrm.10567.

Varallyay, C.G., Nesbit, E., Fu, R., Gahramanov, S., Moloney, B., Earl, E., Muldoon, L.L., Li, X., Rooney, W.D., Neuwelt, E.A., 2013. High-resolution steady-state cerebral blood volume maps in patients with central nervous system neoplasms using ferumoxytol, a superparamagnetic iron oxide nanoparticle. J. Cereb. Blood Flow. Metab. 33, 780–786. https://doi.org/10.1038/jcbfm.2013.36.

Varallyay, C.G., Toth, G.B., Fu, R., Netto, J.P., Firkins, J., Ambady, P., Neuwelt, E.A., 2017. What does the boxed warning tell us? Safe practice of using ferumoxytol as an MRI CONTRAST AGENT. Am. J. Neuroradiol. 38, 1297–1302. https://doi.org/10.3174/ajnr.A5188.

Vasanawala, S.S., Nguyen, K.-L., Hope, M.D., Bridges, M.D., Hope, T.A., Reeder, S.B., Bashir, M.R., 2016. Safety and technique of ferumoxytol administration for MRI. Magn. Reson. Med. 75, 2107–2111.

Vidarsson, L., Thornhill, R.E., Liu, F., Mikulis, D.J., Kassner, A., 2009. Quantitative permeability magnetic resonance imaging in acute ischemic stroke: how long do we need to scan? Magn. Reson. Imaging 27, 1216–1222. https://doi.org/10.1016/j.mri.2009.01.019.

Villringer, A., Rosen, B.R., Belliveau, J.W., Ackerman, J.L., Lauffer, R.B., Buxton, R.B., Chao, Y. S., Wedeenand, V.J., Brady, T.J., 1988. Dynamic imaging with lanthanide chelates in normal brain: contrast due to magnetic susceptibility effects. Magn. Reson. Med. 6, 164–174. https://doi.org/10.1002/mrm.1910060205.

Vonken, E., van Osch, M., Bakker, C., Viergever, M., 1999. Measurement of cerebral perfusion with dual-echo multi-slice quantitative dynamic susceptibility contrast MRI. J. Magn. Reson. Imaging 10, 109–117.

Vonken, E.P.A., van Osch, M.J.P., Bakker, C.J.G., Viergever, M.A., 2000. Simultaneous quantitative cerebral perfusion and Gd-DTPA extravasation measurement with dual-echo dynamic susceptibility contrast MRI. Magn. Reson. Med. 43, 820–827. https://doi.org/10.1002/1522-2594(200006)43:6<820::AID-MRM7>3.0.CO;2-F.

Wang, H., Golob, E.J., Su, M.Y., 2006. Vascular volume and blood-brain barrier permeability measured by dynamic contrast enhanced MRI in hippocampus and cerebellum of patients with MCI and normal controls. J. Magn. Reson Imaging 24, 695–700. https://doi.org/10.1002/jmri.20669.

Wang, Y.-X.J., Hussain, S.M., Krestin, G.P., 2001. Superparamagnetic iron oxide contrast agents: physicochemical characteristics and applications in MR imaging. Eur. Radiol. 11, 2319–2331. https://doi.org/10.1007/s003300100908.

Warach, S.J., Luby, M., Albers, G.W., Bammer, R., Bivard, A., Campbell, B.C.V., Derdeyn, C., Heit, J.J., Khatri, P., Lansberg, M.G., Liebeskind, D.S., Majoie, C.B.L.M., Marks, M.P., Menon, B.K., Muir, K.W., Parsons, M.W., Vagal, A., Yoo, A.J., Alexandrov, A.V., Baron, J.C., Fiorella, D.J., Furlan, A.J., Puig, J., Schellinger, P.D., Wintermark, M., 2016. Acute stroke imaging research roadmap III imaging selection and outcomes in acute stroke reperfusion clinical trials: consensus recommendations and further research priorities. Stroke 47, 1389–1398. https://doi.org/10.1161/STROKEAHA.115.012364.

Weber, M.-A., Thilmann, C., Lichy, M.P., Günther, M., Delorme, S., Zuna, I., Bongers, A., Schad, L.R., Debus, J., Kauczor, H.-U., Essig, M., Schlemmer, H.-P., 2004. Assessment of irradiated brain metastases by means of arterial spin-labeling and dynamic susceptibility-weighted contrast-enhanced perfusion MRI: initial results. Invest. Radiol. 39, 277–287. https://doi.org/10.1097/01.rli.0000119195.50515.04.

Weisskoff, R., Zuo, C.S., Boxerman, J.L., Rosen, B.R., 1994. Microscopic susceptibility variation and transverse relaxation: theory and experiment. Magn. Reson. Med. 31, 601–610. https://doi.org/10.1002/mrm.1910310605.

Weissleder, R., Bogdanov, A., Neuwelt, E.A., Papisov, M., 1995. Long-circulating iron oxides for MR imaging. Adv. Drug Deliv. Rev. https://doi.org/10.1016/0169-409X(95)00033-4.

Welker, K., Boxerman, J., Kalnin, A., Kaufmann, T., Shiroishi, M., Wintermark, M., 2015. American society of functional Neuroradiology, M.R.P.S., practice subcommittee of the, A.C.P.C. In: ASFNR Recommendations for Clinical Performance of MR Dynamic Susceptibility Contrast Perfusion Imaging of the Brain. AJNR Am. J. Neuroradiol, vol. 36, pp. E41–E51. https://doi.org/10.3174/ajnr.A4341.

Willats, L., Calamante, F., 2013. The 39 steps: evading error and deciphering the secrets for accurate dynamic susceptibility contrast MRI. Nmr Biomed. 26, 913–931. https://doi.org/10.1002/nbm.2833.

Willats, L., Christensen, S.K., Ma, H.A., Donnan, G., Connelly, A., Calamante, F., 2011. Validating a local arterial input function method for improved perfusion quantification in stroke. J. Cereb. Blood Flow. Metab. 31, 2189–2198. https://doi.org/10.1038/jcbfm.2011.78.

Wu, E.X., Tang, H., Jensen, J.H., 2004. High-resolution MR imaging of mouse brain microvasculature using the relaxation rate shift index Q. NMR Biomed. 17, 507–512. https://doi.org/10.1002/nbm.921.

Wu, O., Østergaard, L., Weisskoff, R.M., Benner, T., Rosen, B.R., Sorensen, A.G., 2003. Tracer arrival timing-insensitive technique for estimating flow in MR perfusion-weighted imaging using singular value decomposition with a block-circulant deconvolution matrix. Magn. Reson. Med. 50, 164–174. https://doi.org/10.1002/mrm.10522.

Wuerfel, J., Bellmann-Strobl, J., Brunecker, P., Aktas, O., McFarland, H., Villringer, A., Zipp, F., 2004. Changes in cerebral perfusion precede plaque formation in multiple sclerosis: a longitudinal perfusion MRI study. Brain 127, 111–119. https://doi.org/10.1093/brain/awh007.

Yankeelov, T.E., Gore, J.C., 2009. Dynamic contrast enhanced magnetic resonance imaging in oncology: theory, data acquisition, analysis, and examples. Curr. Med. Imaging Rev. 3, 91.

Ye, Y., Hu, J., Wu, D., Haacke, E.M., 2013. Noncontrast-enhanced magnetic resonance angiography and venography imaging with enhanced angiography. J. Magn. Reson. Imaging 38, 1539–1548. https://doi.org/10.1002/jmri.24128.

Yoon, H., Park, S.H., Ye, J.C., 2014. Improved volumetric imaging for DCE-MRI using parallel imaging and dynamic compressed sensing. In: 2014 IEEE Global Conference on Signal and Information Processing (GlobalSIP), pp. 483–486. https://doi.org/10.1109/GlobalSIP.2014.7032164.

Zhao, J., Yang, Z.Y., Luo, B.N., Yang, J.Y., Chu, J.P., 2015. Quantitative evaluation of diffusion and dynamic contrast-enhanced MR in tumor parenchyma and peritumoral area for distinction of brain tumors. PLoS One 10, e0138573. https://doi.org/10.1371/journal.pone.0138573.

Zhu, Y., Guo, Y., Lingala, S.G., Barnes, S., Lebel, R.M., Law, M., Nayak, K., 2015. Evaluation of DCE-MRI data sampling, reconstruction and model fitting using a digital brain phantom. In: Proceedings of the 23rd Annual Meeting of ISMRM. Toronto, Ontario, Canada, p. 3070.